Squashing Crystals with the Big Felsic Enclave: Magma Dynamics in the Aztec Wash Pluton

By

Elizabeth C. Teeter

Thesis

Submitted to the Faculty of the

Graduate School of Vanderbilt University

in partial fulfillment of the requirements

for the degree of

MASTER OF SCIENCE

in

Earth and Environmental Sciences

December 18, 2021

Nashville, Tennessee

Approved:

Guilherme A.R. Gualda, Ph.D.

Kristen E. Fauria, Ph.D.

ACKNOWLEDGMENTS

This material is based upon work supported by the National Science Foundation Graduate Research Fellowship Program under Grant No. 1937963. Any opinions, findings, and conclusions or recommendations expressed in this material are those of the author and do not necessarily reflect the views of the National Science Foundation. I would also like to thank Nick Hinz for collecting the four samples analyzed in this study.

TABLE OF CONTENTS

Page

LIST OF TABLES . . . . . **iv**

LIST OF FIGURES . . . . . **v**

1 Introduction **1**

1.1 Overview 1
1.2 Geologic Background 2
1.2.1 Aztec Wash Pluton 2
1.2.2 Enclave Formation 3
1.2.3 The Big Felsic Enclave (BFE) and Magma Deformation 4

2 Methods **7**

3 Results **13**

3.1 Backscatter Electron (BSE) 13
3.2 Energy Dispersive Spectrometry (EDS) 16
3.3 Electron Backscattered Diffraction (EBSD) 20

4 Discussion **23**

4.1 Evidence of deformation 23
4.2 Compaction beneath the BFE 26
4.3 Length scale of compaction 27
4.4 Evidence of melt extraction 28

5 Conclusions **29**

References **30**

LIST OF TABLES

Table		Page
1	EBSD mineral percentages.	21

LIST OF FIGURES

Figure		Page
1	Geologic map of Aztec Wash showing the location of the Big Felsic Enclave (BFE) – the red X – in the GZ cumulate (Granite Zone). Modified from Harper et al. (2004). The location of the Aztec Wash Pluton in Nevada is marked by the orange star in the inset. . .	3
2	Field photograph showing the Big Felsic Enclave in contact with the host granite. The BFE is fine grained, slightly more mafic than the surrounding granite. It is approximately equant and it is 2 m in diameter. Sample locations analyzed in this study are marked by red arrows. The fabric observed in the field is directly underneath the enclave, by E-5 and E-2. There is no observed fabric in the far field at sample E-3. Samples E-1 and E-4 were not studied in detail. A Diagram of the BFE showing sample locations relative to the BFE is located at the bottom right. This image will be used in later figures to indicate which sample is being analyzed.	5
3	Sample locations for E-5 and E-2, underneath the BFE. Note that directly underneath the enclave, we can observe an oriented fabric in the alkali feldspars, parallel to the base of the BFE. The sampling locations of E-5 and E-2 aim to capture this fabric.	6
4	BSE image of full thin section of sample E-5. Gray scale in the BSE images was optimized to show the main phases (quartz, plagioclase, and alkali feldspar). Quartz (dark gray), plagioclase (medium gray), and alkali feldspar (light gray) are most abundant. Accessory minerals (i.e. zircon, magnetite, apatite, titanite) are very bright gray or white.	8
6	Examples of unit cell orientations and corresponding Kikuchi patterns for selected grains. A and B show two plagioclase grains in different orientations. C shows an example of alkali feldspar, while D shows an example of quartz.	9
7	EBSD maps for full thin section of sample E-5. A. Band Contrast maps show the different grains within the sample. B. Phase maps show each mineral phase in a different color: alkali feldspar are red, plagioclase are blue, and quartz are grey. C. Euler maps show the orientation of individual grains of a phase; each color represents a different orientation. D. GOS maps show intragrain deformation in plagioclase; red=higher degree of intragrain deformation.	10
8	Visual representation of θ showing the angle between the vertical vector (current vertical direction) and the pole to the (010) plane used to demonstrate the strength of foliation in the alkali feldspar phase. A strong foliation occurs when all the (010) poles are clustered near the same location.	11
9	BSE maps of all four thin sections. Some of the visible alkali feldspar zones are outlined in red, and some of the alkali feldspar rims are outlined in blue. Alkali feldspar are lighter gray, plagioclase are medium gray, and quartz are darker gray. A. Map of E-5, located directly underneath the BFE: most alkali feldspar are euhedral with distinct zoning patterns. Plagioclase are generally smaller than the alkali feldspar and quartz is primarily interstitial. B. Map of E-2, located next to E-5 underneath the BFE. Large euhedral alkali feldspar (¡10mm) primarily make up the map. Plagioclase are euhedral, but they are smaller than the alkali feldspar; quartz is interstitial. C. BSE map of E-6, located underneath E-5: alkali feldspar are anhedral; zones are outlined in red. There is a large plagioclase cluster in the center of the sample and there are alkali feldspar grains with distinct plagioclase zones within the grains. D. BSE map of E-3, located in the far field. E-3 is texturally distinct from E-5 and E-2 (both have large euhedral alkali feldspar). The most notable features are the irregular alkali feldspar rims. These rims are tendril-like and are darker grey than the rest of the alkali feldspar grains.	15

10 BSE images of four interesting feldspar textures. Internal zoning is outlined in red and rims are outlined in blue. A. Plagioclase cluster in E-5 (directly underneath the enclave) shows bent grains. B. In E-2, a large alkali feldspar grain is broken. We can observe three domains within the grain, with the wedge-shape zone interrupting the zoning seen in the outer domains. C. Example of an irregular alkali feldspar rim in E-3 (located in the far field). There are distinct euhedral zones within the grain, but the rim is irregular with tendrils of material interstitial to matrix grains. This rim texture is abundant in sample E-3, while the euhedral grains (such as the one in 11B) are common in samples E-5 and E-2. In other alkali feldspar in the sample, as well as this example, the rims are darker than the interior of the grain. D. Alkali feldspar with plagioclase zone in E-6 (underneath the E-5). These zones of plagioclase are common in all four of the samples. 16
11 False color EDS map of all four samples. A. E-5, B. E-2, C. E-3, and D. E-6. Alkali feldspar grains are green and plagioclase grains are purple. Zoning can be seen clearly within the plagioclase grains. Alkali feldspar zoning is still visible, but not as clear as in the BSE images. Plagioclase inclusions and zones can be seen clearly in these false color maps. A. In E-5, inclusions and zones of plagioclase can be observed within the euhedral alkali feldspar. B. Alkali feldspar zoning is seen within E-2 in the large euhedral grains along with the plagioclase inclusions and zones seen in other samples. C. In E-3, the irregular rims observed in the BSE image can be seen in this EDS map as well. D. Similarly to the other samples, zoning in E-6 can be observed in this EDS map. Additionally, the large plagioclase cluster in the middle of the image can be seen in greater detail. Individual grains within the cluster are more visible, and we can see a rim surrounding the majority of the cluster that is more Ca-rich. 19
12 Ba EDS maps and BSE images showing zoning in alkali feldspar in sample E-3. Ba EDS maps on top, in shades of red, while BSE images are on the bottom, in shades of gray. We observe that the BSE dark, irregular rims are Ba-depleted, compared to the Ba-rich, BSE bright cores. This can be seen more clearly in the zoomed-in maps of a large alkali feldspar grain located to the right of the thin section. The zones that are visible and outlined in the BSE map match with the area of the grain that is Ba-rich in the EDS map. These darker rims can in found on the other samples, but they are much smaller and harder to observe with an EDS map. 20
13 Grain Spread Orientation (GOS) angle vs. grain diameter in alkali feldspar show intragrain deformation in alkali feldspar grains of different sizes for the four samples. GOS measures how much variability in orientation there is within pixels of each grain; a larger angle implies that the grain is more deformed. All the samples look remarkably similar to each other in these plots. While there are a few large grains in E-5 and E-6 that are more deformed, there does not appear to be a great difference. It is important to note that the sample size for the smaller grains is much higher than the large grains and therefore the deformation shown here may not be representative of the granite in each of these locations. 22
14 Histograms showing the foliation strength in the four samples. A sample with a strong foliation would have a tightly clustered unimodal distribution of θ, while a sample with no foliation would show a uniform distribution of θ. E-5 has the strongest foliation, while E-2 appears to have a weaker foliation. E-6 and E-3 appear to have a bimodal distribution; however, further statistical analysis must be done to confirm this pattern. Interestingly, each sample is foliated, with E-5 having the strongest foliation. 22

15 Analysis of the bent grain in E-2 with BSE (A), EDS (B), Euler angles (C), and GOS (D). All four visualizations of this large grain show that there are different domains. The Euler map (C) shows that the different domains observed in the BSE image are true orientation differences. The different orientation domains are outlined in black. Note that there is twinning occurring in the top domain (brown/purple) and the lower domain (green/blue); these orientation differences are due to normal crystal growth, not deformation. The GOS map (D) also shows the different domains. The lower domain is the most deformed, with three areas within the wedge of the two main domains having no intragrain deformation. This data shows that the grain broke, and new growth (3 wedge domains) may have occurred after the breakage. 24
16 BSE (A) and Euler (B) maps of plagioclase cluster in E-5 showing the three different orientation domains in the top plagioclase grain, indicating that this grain broke into three pieces. Other bent grains within the cluster do not have subgrains within them and may have undergone ductile rather than brittle deformation. 25
17 GOS map of E-5 showing intragrain deformation in alkali feldspar grains (A) vs. quartz grains (B). The alkali feldspar grains have more intragrain deformation than the quartz grains. This difference indicates that quartz grew after the feldspar were deformed. . . . 26

CHAPTER 1

Introduction

1.1 Overview

The connection between magmatic and volcanic systems is key to understanding eruptions; however, studying magma bodies poses significant challenges. The presence of melt, crystals, and bubbles complicates the mechanical behavior of magma. However, one of our primary sources of evidence for these behaviors, plutons (crystallized magma bodies) preserve long histories but may erase dynamics through time (Bachmann et al., 2007; Hildreth, 2004; Mader et al., 2013). Therefore, analyzing how volcanic eruptions are generated from magma bodies is difficult. In our current understanding, magma bodies contain both melt and crystals and varying concentrations of crystals will cause the magma to behave differently: increasing crystallinity will cause increasing viscosity (Hess and Dingwell, 1996; Hildreth, 2004; Marsh, 1981). While there is no simple crystal fraction that determines the behavior of the magma, evidence indicates that there is a boundary between a melt-rich portion of a magma body and a crystal-rich portion that behaves like a solid as opposed to a fluid (Hildreth, 2004; Marsh, 1981; Mader et al., 2013; Miller et al., 1988; Weinberg et al., 2021). Crystal mushes were originally conceptualized to have a higher crystal fraction than eruptible magma, while still behaving as a fluid (15-25 to 50-60% crystal fraction) (Hildreth, 2004; Marsh, 1981). However, in this paper I use a modified definition from Weinberg et al., 2021 and consider a crystal mush to exist where a high crystal fraction causes the magma to behave rigidly (typically $\geq$ approximately 50-60%). High crystal contents in a magma body impact how a magma deforms and flows and understanding these changes will aid in our understanding of magmatic processes (Mader et al., 2013; Mueller et al., 2011).

The relationship between stress and the rate of deformation (i.e., rheology) is essential to understand how magma flows and erupts (Giordano et al., 2008; Mader et al., 2013; Mueller et al., 2011). While the viscosity and rheology of pure melt is well known, the addition of crystals changes how magma behaves (Giordano et al., 2006; Marsh, 1981; Webb and Dingwell, 1990). Crystal packing fraction, grain size, and grain shape all impact magma rheology (Mueller et al., 2011; Saar et al., 2001). While a pure melt can be modelled as a Newtonian fluid, high concentrations of crystals generate non-Newtonian behavior (Coussot and Ancey, 1999; Mader et al., 2013; Mueller et al., 2011; J.J.Stickel and Powell, 2005). Connecting magma rheology to magmatic processes evidenced in plutonic rocks is a challenge in igneous petrology.

Plutonic rocks preserve evidence of the lifetime of a magmatic system, and they thus provide an integrated record of crystallization (Bachmann et al., 2007); however, they do not provide clear snapshots into how the

behavior of magma changes with increasing crystallization. Studies that connect evidence found in plutons to magma rheology evolution can provide insight on magma mingling and mixing, rejuvenation events, enclave formation, and melt extraction using geochemical techniques as well as in depth textural analyses (Harper et al., 2004; Wiebe et al., 2007; Weinberg et al., 2021). Magmatic fabrics recorded in plutonic rocks can be used to understand aspects of such magma dynamics (Holness, 2018; Ji et al., 2014; Žák et al., 2008). Fabrics can indicate magmatic deformation; however, it is a challenge to connect an oriented fabric with the stress that generated it.

The Aztec Wash pluton (southern Nevada, USA) provides a unique opportunity to connect observed magmatic fabrics to a known stress by looking at a fabric generated beneath a large felsic enclave within a coarse granite host. In this study I identify and quantify an oriented fabric underneath the enclave and explore how this fabric changes in the granitic rocks relative to the enclave location. The fabric characteristics yield insights into the rheology of the mush and mush deformation process.

1.2 Geologic Background

1.2.1 Aztec Wash Pluton

The Aztec Wash pluton is located in the Eldorado Mountains of southern Nevada, 80 km south of Las Vegas (Falkner et al., 1995). It is exposed within the northern Colorado River extensional corridor, in which east-west extension occurred between 16 and 13 Ma. Regional volcanism spanned a longer interval, beginning around 20 Ma and ending around 8 Ma (Faulds et al., 2001; Harper et al., 2004). The pluton was emplaced near the onset of extension, between 15.5 and 15.8 Ma (Cates et al., 2003; Leigh et al., 2018).

The Aztec Wash pluton is of particular interest and use because it is within a crustal block that was tilted up to 90 degrees and thus exposes a cross section through the pluton (Faulds et al., 2001; Harper et al., 2004; Miller et al., 2005; Miller and Miller, 2002). The pluton is generally divided into two main zones (see Figure 1). The heterogeneous zone has been the focus of many studies and it includes rocks of varying composition from troctolites and quenched basalts to leucogranites (Harper et al., 2004). The granite zone is more homogeneous in composition, but it also records dynamic cumulate processes (Harper et al., 2004). Harper et al. (2004) interpret the granite zone to have been constructed through a series of episodes of upward accumulation of crystals, interrupted by pulses of injection of mafic magma that interacted with granitic material in the heterogeneous zone. Fine-grained felsic enclaves with a slightly more mafic composition than the surrounding host granite are found throughout the granite zone (Harper et al., 2004; Lazzareschi, 2004). While the origins of the enclaves in the Aztec Wash pluton are not the primary concern for this study, their emplacement into the granite is important to note as it pertains to the interpretation of the evidence presented in this thesis.

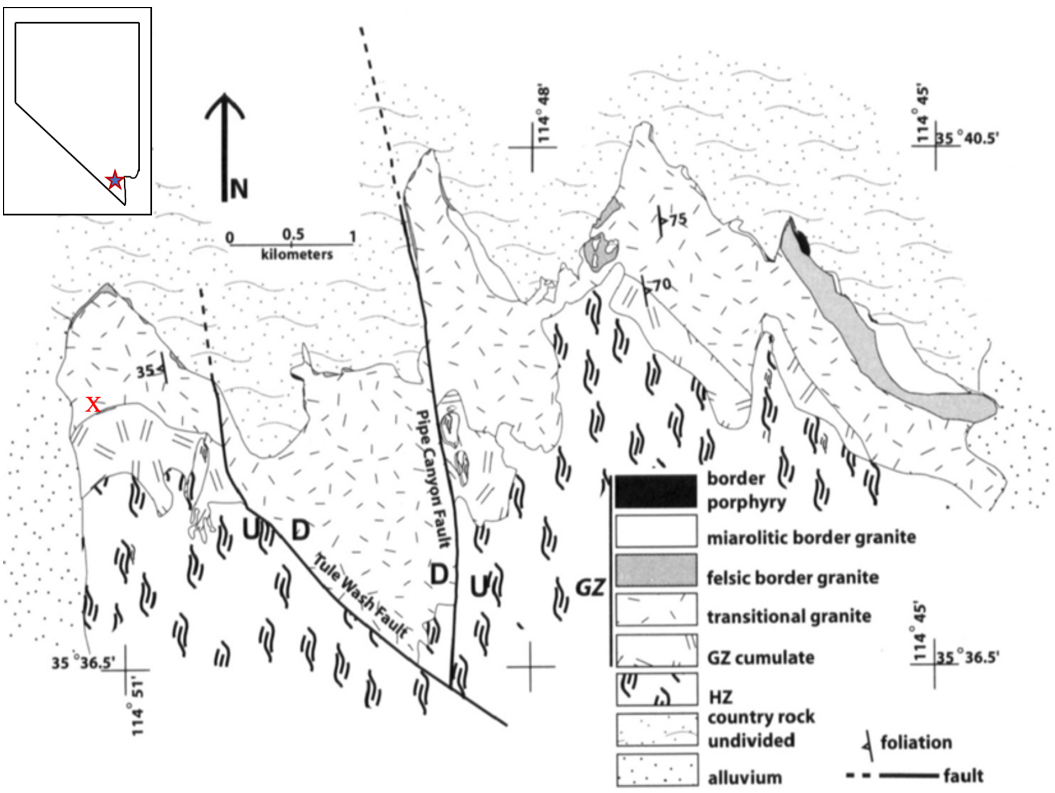

Figure 1: Geologic map of Aztec Wash showing the location of the Big Felsic Enclave (BFE) – the red X – in the GZ cumulate (Granite Zone). Modified from Harper et al. (2004). The location of the Aztec Wash Pluton in Nevada is marked by the orange star in the inset.

1.2.2 Enclave Formation

Multiple types of enclaves exist in the granite zone of Aztec Wash; however, this study will focus on the abundant fine-grained felsic enclaves (Harper et al., 2004; Lazzareschi, 2004). An in-depth study of these enclaves has not been published. However, Danny Lazzareschi's thesis from Pomona College presents compelling evidence on their formation. The main findings that are relevant to this study are:

1. The composition of the enclaves is between 68% and 72 wt% SiO2, and are thus more mafic than the host granite.

2. The enclaves are very fine-grained to aphanitic, contrasting to the coarse-grained host granite.

3. The compositions and textures of the enclaves imply that they were not formed in place, rather they were transported throughout the magma body.

From very fine-grained to aphanitic, the textures of these enclaves contrast with the host granite, implying that they are quenched melt (Lazzareschi 2004). Typical enclaves are ovoid and range from 5 to 20 cm in

diameter (Lazzareschi 2004). The composition of the enclaves is clustered between 68% and 72% SiO2, contrasting to the composition of the host granite whose composition is mostly 72%-74% SiO2 (Lazzareschi 2004). This compositional difference implies that the enclaves were not fractioned liquids from the granite; textural and compositional differences show that the enclaves were formed by a different process than the granite and they were transported to their final locations (Lazzareschi 2004). The formation of the enclaves and the method of transport to their present locations is not fully understood, but Lazzareschi (2004) presents hypotheses for both questions. Enclave composition indicates that they could have been formed in or at the margin of the heterogeneous zone as well-mixed hybrids rich in a granitic end member (Lazzareschi 2004). Alternatively, the enclaves could be quenched margin materials (Lazzareschi 2004). Understanding how the enclaves were transported through the magma body is challenging, but Lazzareschi (2004) hypothesizes that some of the enclaves formed from the dissociation of felsic hybrid dikes within the granite or that they were material carried off the heterogeneous zone by gravity or convection. While the formation of the enclaves is not thoroughly understood, it is important to note that the enclaves were transported and then deposited throughout much of the granitic portion of the magma body (Lazzareschi 2004). In this study, I will focus on the largest enclave observed (approximately 2 m diameter) and the textures of the surrounding granite.

1.2.3 The Big Felsic Enclave (BFE) and Magma Deformation

The BFE is visibly distinct from the surrounding coarse-grained granite, and it appears light grey (Figure 2). Field observations reveal that the feldspar crystals directly underlying the enclave appear aligned, with a preferred orientation forming a nearly horizontal foliation (Figure 3); feldspar crystals some distance from the enclave do not appear to have an oriented fabric. These field observations suggest that the BFE may be located at a past interface between the mush portion of the magma body and the crystal-poor, melt-rich portion (Wiebe et al., 2007; Wiebe and W.J.Collins, 1998). In this study, I analyze samples from underneath the enclave and in the far field from the enclave to understand the effect of the emplacement of the enclave into the granite. The primary questions guiding this study are as follows:

1. What evidence is there of deformation in the granite surrounding the enclave?
2. To what extent does a preferred orientation exist and how does this fabric connect to stresses imposed from an enclave moving through magma?

I hypothesize that an oriented fabric exists beneath the enclave and that it results from the impingement of the enclave on a crystal-rich region of a magma body.

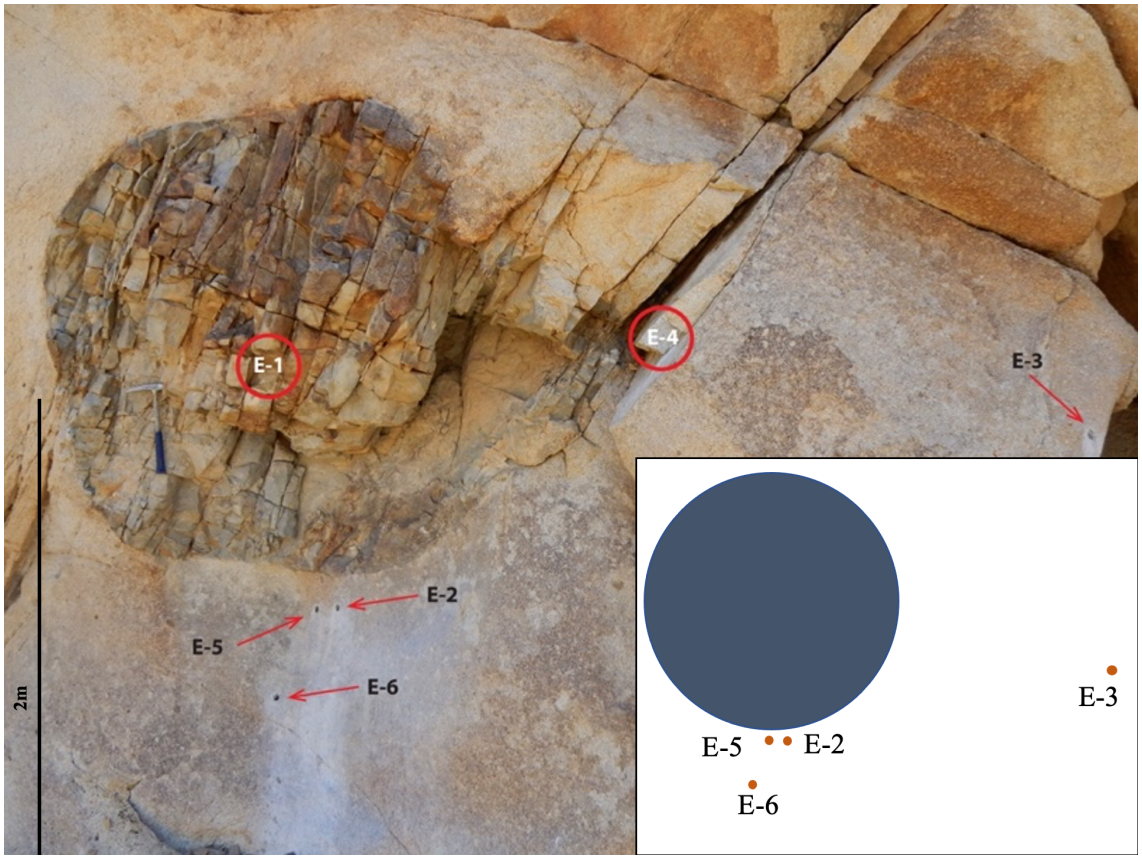

Figure 2: Field photograph showing the Big Felsic Enclave in contact with the host granite. The BFE is fine grained, slightly more mafic than the surrounding granite. It is approximately equant and it is 2 m in diameter. Sample locations analyzed in this study are marked by red arrows. The fabric observed in the field is directly underneath the enclave, by E-5 and E-2. There is no observed fabric in the far field at sample E-3. Samples E-1 and E-4 were not studied in detail. A Diagram of the BFE showing sample locations relative to the BFE is located at the bottom right. This image will be used in later figures to indicate which sample is being analyzed.

Figure 3: Sample locations for E-5 and E-2, underneath the BFE. Note that directly underneath the enclave, we can observe an oriented fabric in the alkali feldspars, parallel to the base of the BFE. The sampling locations of E-5 and E-2 aim to capture this fabric.

CHAPTER 2

Methods

I analyzed four oriented samples for this study. Nick Hinz (then at Nevada Bureau of Mines and Geology, now with Geologica Geothermal Group) collected these four by drilling. Three samples were located underneath the BFE and one in the far field, where no fabric was observed (Figures 2). E-5 was 0.25 m directly underneath the enclave, E-2 is slightly offset to the side of E-5, and E-6 is located 0.5 m underneath the enclave. E-3 was approximately 2.5 m laterally distant from the BFE, and based on its distance and the apparent absence of fabric I consider it to be far field sample.

Samples were collected using a rock drill, with the direction of the core being within the plane of the foliation observed in the field. All cores were approximately parallel to each other. Each sample was cut along the length of the core, along a plane perpendicular to the foliation, to best expose the alignment of crystals in the rock. Current vertical is along the plane of the thin section and each image of the samples are oriented with "up" as current vertical. Sectioned rocks were sent to Precimat to be made into thin sections. The four thin sections were prepared for SEM data collection with a colloidal silica polish using a Buehler Vibromet for 2 hours to improve electron diffraction, and a carbon coat was applied to prevent electron charging effects during SEM analysis.

I used a TESCAN Scanning Electron Microscope (SEM) at Vanderbilt University for the Backscatter Electron (BSE) detector and I used Aztec 4.1 software from Oxford Instruments for Energy Dispersive Spectrometry (EDS) and the Electron Backscatter Diffraction (EBSD) technique.

For BSE, I set up full thin section maps with 15 kV, 20 Beam Intensity (BI), and 15 mm Working Distance (WD) as the parameters. The brightness and contrast were optimized to best show alkali feldspar, plagioclase, and quartz and these parameters varied depending on the different thin sections (Figure 4). I set up full thin section maps as a montage of tens to hundreds of individual images of size 512 x 512 μm; each map took 4-6 hours to collect. We wrote a routine in IDL to stitch together the frames to create the full map.

EDS quantifies the composition of the sample based on the concentration of different elements within the sample (Figure 5). I set up EDS maps with 15 kV, 20 BI, 15 mm WD, and 2048 x 2048 μm for the view field to set up full thin section maps. Utilizing the Aztec software, I chose 25 frames per view field with a dwell time of 7 µs per pixel per frame. Each map took 10 hours. The images were stitched together using the Aztec software (the Montage feature). I applied an IDL routine to create false-color maps for each sample with different elements as individual color channels (K is green, Na is blue, and Ca is red). I chose these elements because they predominantly make up plagioclase and alkali feldspar and show zoning patterns.

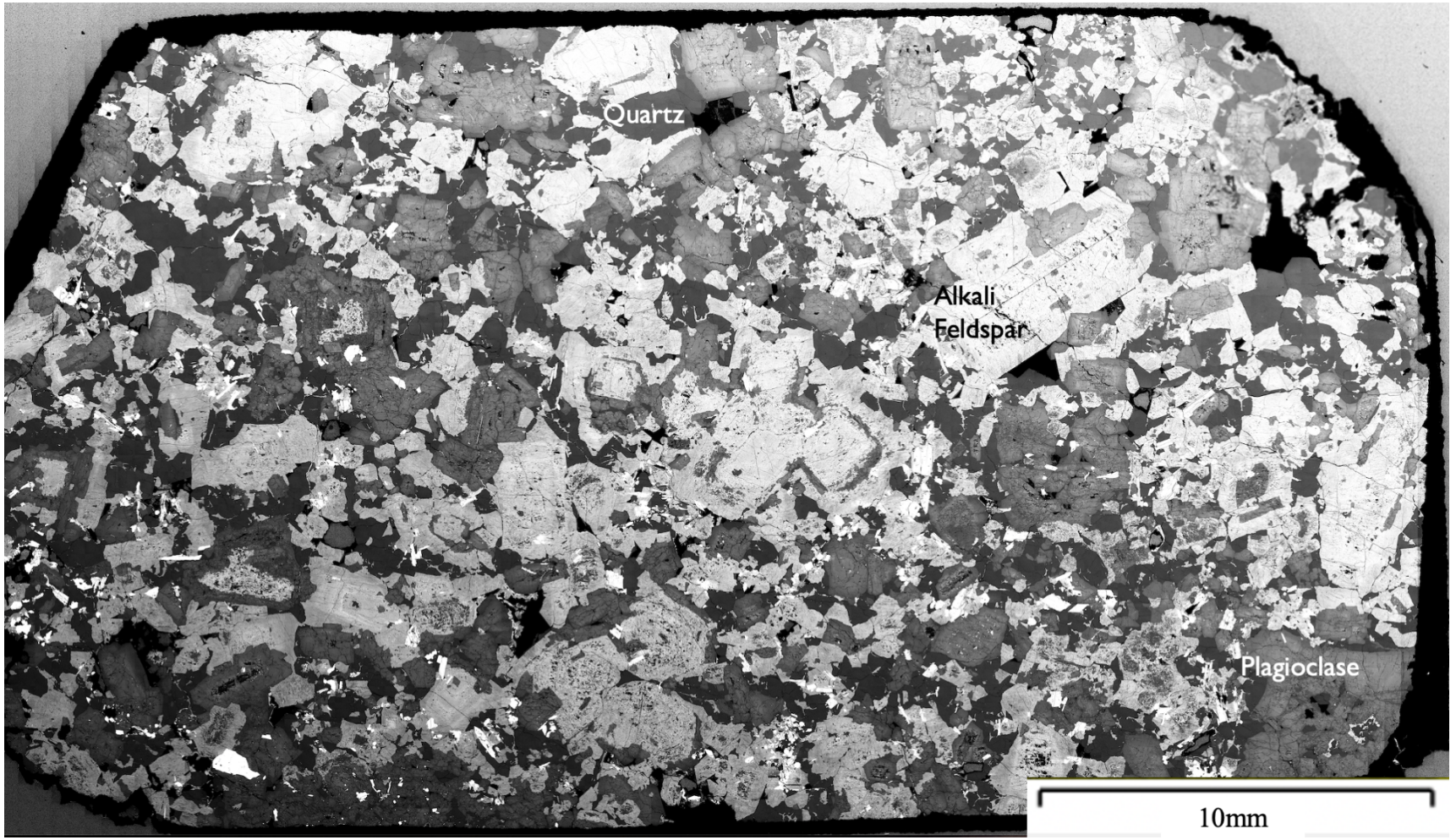

Figure 4: BSE image of full thin section of sample E-5. Gray scale in the BSE images was optimized to show the main phases (quartz, plagioclase, and alkali feldspar). Quartz (dark gray), plagioclase (medium gray), and alkali feldspar (light gray) are most abundant. Accessory minerals (i.e. zircon, magnetite, apatite, titanite) are very bright gray or white.

The EBSD detector quantifies magmatic fabrics by collecting the orientations of individual crystal grains in a thin section to show the crystallographic preferred orientation and shape preferred orientation of the whole sample (Prior et al., 1999). It can also quantify the change in orientation within a single grain. The EBSD detects diffraction patterns that identify different mineral phases and different 3D crystallographic orientations (Figure 6). We can use the crystallographic preferred orientation (CPO) to tie textures to different plutonic processes (Beane and Wiebe, 2012; Graeter et al., 2015; Ji et al., 2014; Žák et al., 2008).

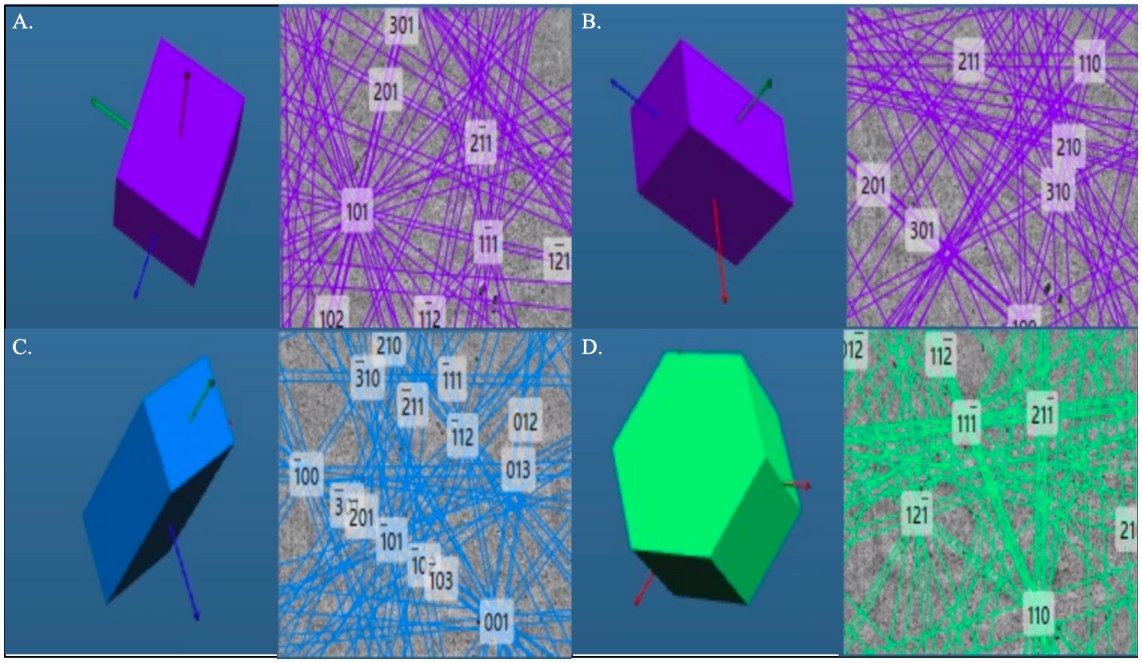

Figure 6: Examples of unit cell orientations and corresponding Kikuchi patterns for selected grains. A and B show two plagioclase grains in different orientations. C shows an example of alkali feldspar, while D shows an example of quartz.

With the configuration of the Vanderbilt SEM, it is only possible to collect data for one half of a thin section at a time. The samples were tilted to 70 degrees and the SEM parameters are 20 kV, 20 BI, 15 mm WD, and a 1000 μm view field. For band image optimization in Aztec, I used 2x2 binning, with a 300 ms exposure time. I set up my maps with a 30 µm step size (pixel size) and 1000 µm wide frame. In each half of a thin section, there were 400 frames and the maps took 30 hours. I collected EDS maps at the same time to help with the mineral indexing. The phases I chose to index are sanidine, anorthite, and quartz. Zero solutions for EBSD indexing are pixels that were not able to be categorized as any of these phases.

I processed the EBSD data with Channel5 and the program Tango to create band contrast maps, phase maps, Euler angle maps, and Grain Orientation Spread (GOS) maps (Figure 7). I performed the noise reduction process to clean up the data and the grain detection process to assign each pixel to an individual grain. I exported the grain list and calculated the rotational matrix for the Euler angles to quantify the orientations of

each grain relative to vertical.

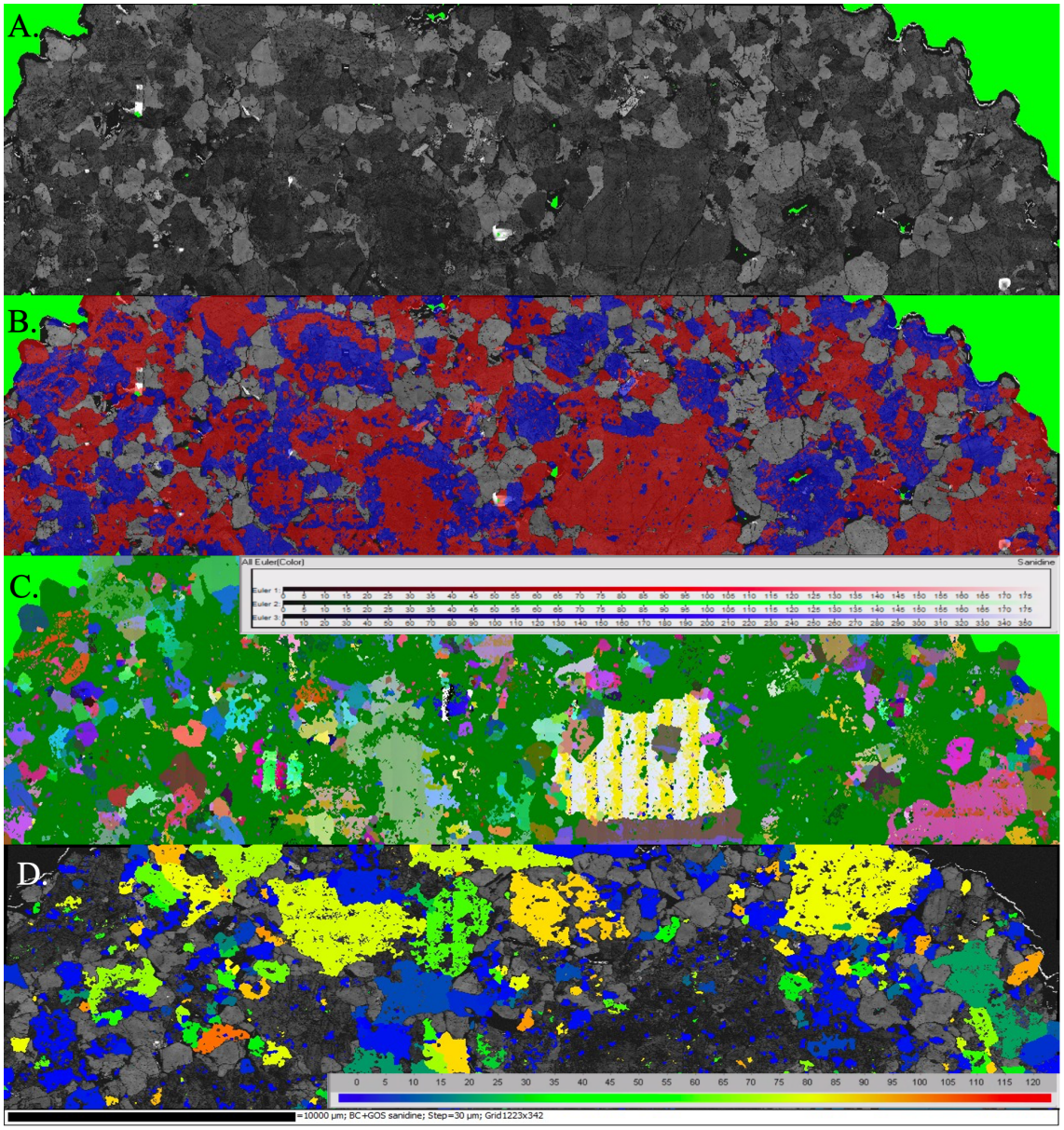

Figure 7: EBSD maps for full thin section of sample E-5. A. Band Contrast maps show the different grains within the sample. B. Phase maps show each mineral phase in a different color: alkali feldspar are red, plagioclase are blue, and quartz are grey. C. Euler maps show the orientation of individual grains of a phase; each color represents a different orientation. D. GOS maps show intragrain deformation in plagioclase; red=higher degree of intragrain deformation.

The Euler angles represent the 3D orientation of each grain within space, relative to the thin section. At the location of the BFE, tilting was gentle (15 degrees to the WSW; Harper et al., 2004), and therefore the plane of the thin section is close to paleovertical. For feldspars, the plane that typically shows foliation is (0 1 0) (Deer et al., 2013) I use the pole to the (0 1 0) plane (the vector perpendicular to the plane of interest) to

describe the orientation of each grain. I used the rotational matrix for the Euler angles, Eq. (1, 2), to find the rotated (0 1 0) plane. Then I calculated the angle between the rotated (0 1 0) vector plane and the reference (0 1 0) vector using the dot product shown in Eq. (2, 4). Therefore θm is the angle between the plane of the thin section that is approximately vertical and the (0 1 0) pole (Figure 8). A histogram of θm in a sample will show the strength of the foliation; a sample with a strong foliation will have a tightly clustered symmetrical distribution, while a sample with no orientation should have a completely random histogram.

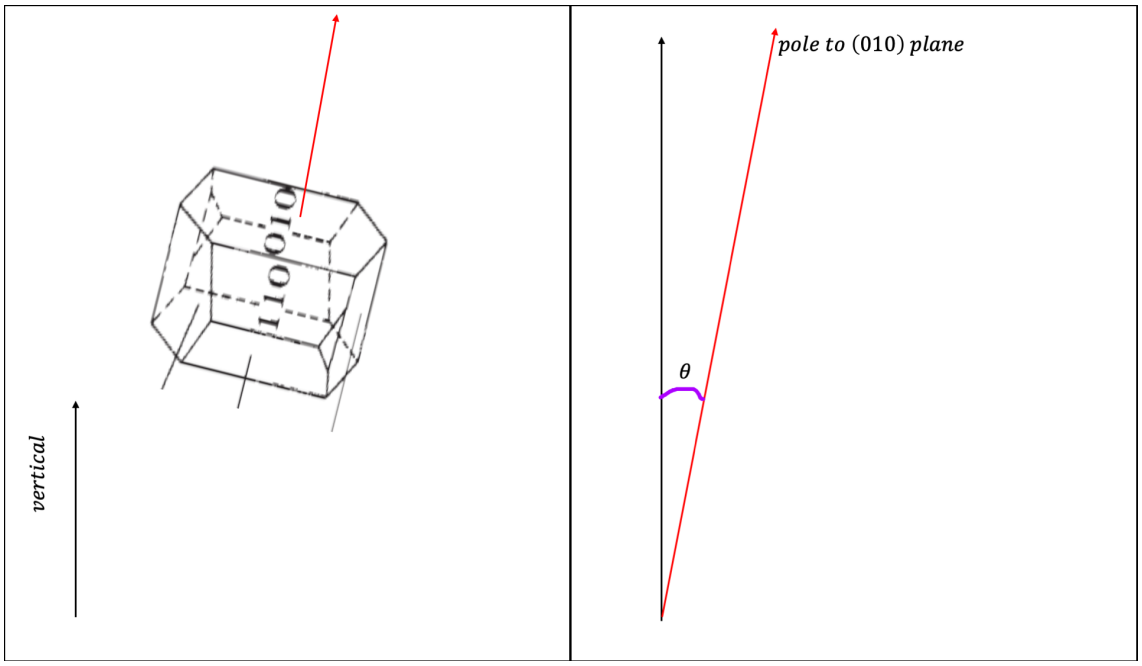

Figure 8: Visual representation of θ showing the angle between the vertical vector (current vertical direction) and the pole to the (010) plane used to demonstrate the strength of foliation in the alkali feldspar phase. A strong foliation occurs when all the (010) poles are clustered near the same location.

$$R(\phi_1,\Phi,\phi_2) = \begin{pmatrix} cos\phi_1 & -sin\phi_1 & 0 \\ sin\phi_1 & cos\phi_1 & 0 \\ 0 & 0 & 1 \end{pmatrix} \begin{pmatrix} 1 & 0 & 0 \\ 0 & cos\Phi & -sin\Phi \\ 0 & sin\Phi & cos\Phi \end{pmatrix} \begin{pmatrix} cos\phi_2 & -sin\phi_2 & 0 \\ sin\phi_2 & cos\phi_2 & 0 \\ 0 & 0 & 1 \end{pmatrix} \tag{1}$$

$$R(\phi_1,\Phi,\phi_2) = \begin{pmatrix} cos\phi_1 cos\phi_2 - sin\phi_1 cos\Phi sin\phi_2 & -cos\phi_1 sin\phi_2 - sin\phi_1 cos\Phi cos\phi_2 & sin\Phi sin\phi_1 \\ sin\phi_1 cos\phi_2 + cos\phi_1 cos\Phi sin\phi_2 & -sin\phi_1 sin\phi_2 + cos\phi_1 cos\Phi cos\phi_2 & -sin\Phi cos\phi_1 \\ sin\Phi sin\phi_2 & sin\Phi cos\phi_2 & cos\Phi \end{pmatrix} \tag{2}$$

$$R\vec{Y} = \vec{y} \tag{3}$$

$$cos^{-1}(\vec{Y} \cdot \vec{y}) = \theta \tag{4}$$

Where R is the rotational matrix for the Euler angles, Y is the present-day vertical vector, y is the rotated pole to the (010) plane, and theta is the angle between the vertical vector and the pole to the (010) plane. For interpretation purposes, it is important to note that paleovertical in this part of the Aztec Wash Pluton is tilted 15 degrees, as previously stated.

CHAPTER 3

Results

3.1 Backscatter Electron (BSE)

Full thin section BSE maps (Figure 9) show different mineral phases as well as key textures within the four thin sections. In each sample the full thin section maps show alkali feldspar (light gray), plagioclase (medium gray), and quartz (dark gray), as well as biotite and accessory minerals – i.e. zircon, magnetite, apatite, titanite (very bright gray or white). Alkali feldspar is the most abundant phase, with the largest grains in each sample; plagioclase grains are also abundant, while quartz, though fairly abundant, is restricted to interstitial positions between feldspars. Zoning in both the alkali feldspar and plagioclase grains can be seen in all four thin sections.

In E-5, there are alkali feldspar grains up to 5 mm in length in the long direction (Figure 9a). Many alkali feldspar grains are euhedral with clear zoning. Similarly, plagioclase grains also are euhedral with less prominent zoning patterns. A plagioclase cluster located in E-5 has two individual grains whose shapes appear to be bent (Figure 10A). In the larger alkali feldspar grains, we can see plagioclase inclusions along zoning boundaries as well as cases where there is a separate plagioclase zone within the alkali feldspar grain. Inclusions and the plagioclase zones can be seen in all four of the thin sections.

In E-2, located underneath the enclave offset from E-5 as seen in figure 2, the alkali feldspar grains have a larger size range, with lengths up to 10 mm in the long direction (Figure 9B). As in E-5, the alkali feldspar grains are euhedral with distinct zoning patterns. In one of the largest grains, the zones appear to be offset in the middle of the crystal and cannot be traced continuously (Figure 10B). Additionally, there appears to be a wedge in the middle-right of the grain that has different zoning. In the larger feldspar grains, we see larger plagioclase inclusions, similarly aligned with the zoning patterns of the grain.

Located farther below the boundary between enclave and granite, E-6 has more plagioclase grains than E-5 and E-2, with a large cluster located in the middle of the sample (Figure 9C). The alkali feldspar grains have visible zoning patterns, but they are not euhedral. Many grains have an anhedral rim surrounding a crystal that is mostly euhedral, as indicated by the zoning pattern. These feldspar grains are smaller than in the first two samples, with lengths up to 4 mm in long dimension.

E-3, the far field sample, is visually distinct from E-5 and E-2 with no euhedral alkali feldspar grains (Figure 9D). Alkali feldspar grains range up to 6 mm in the long direction. In this sample, while the alkali feldspar zones are distinct, the rims are very irregular and wavy (Figure 10C). These irregular rims are similar

to those in E-6, but they are more prominent, especially in the larger grains. Additionally, these irregular rims have a higher mean atomic number (darker gray) than the rest of the grain in all the alkali feldspars within the thin section, indicating a compositional change, potentially in increased Na or lower Ba. Instances of alkali feldspar grains with distinct interior plagioclase zones are common in this sample. These zones are discrete plagioclase rings around an alkali feldspar core, there is also an alkali feldspar rim surrounding the plagioclase zone (Figure 10D).

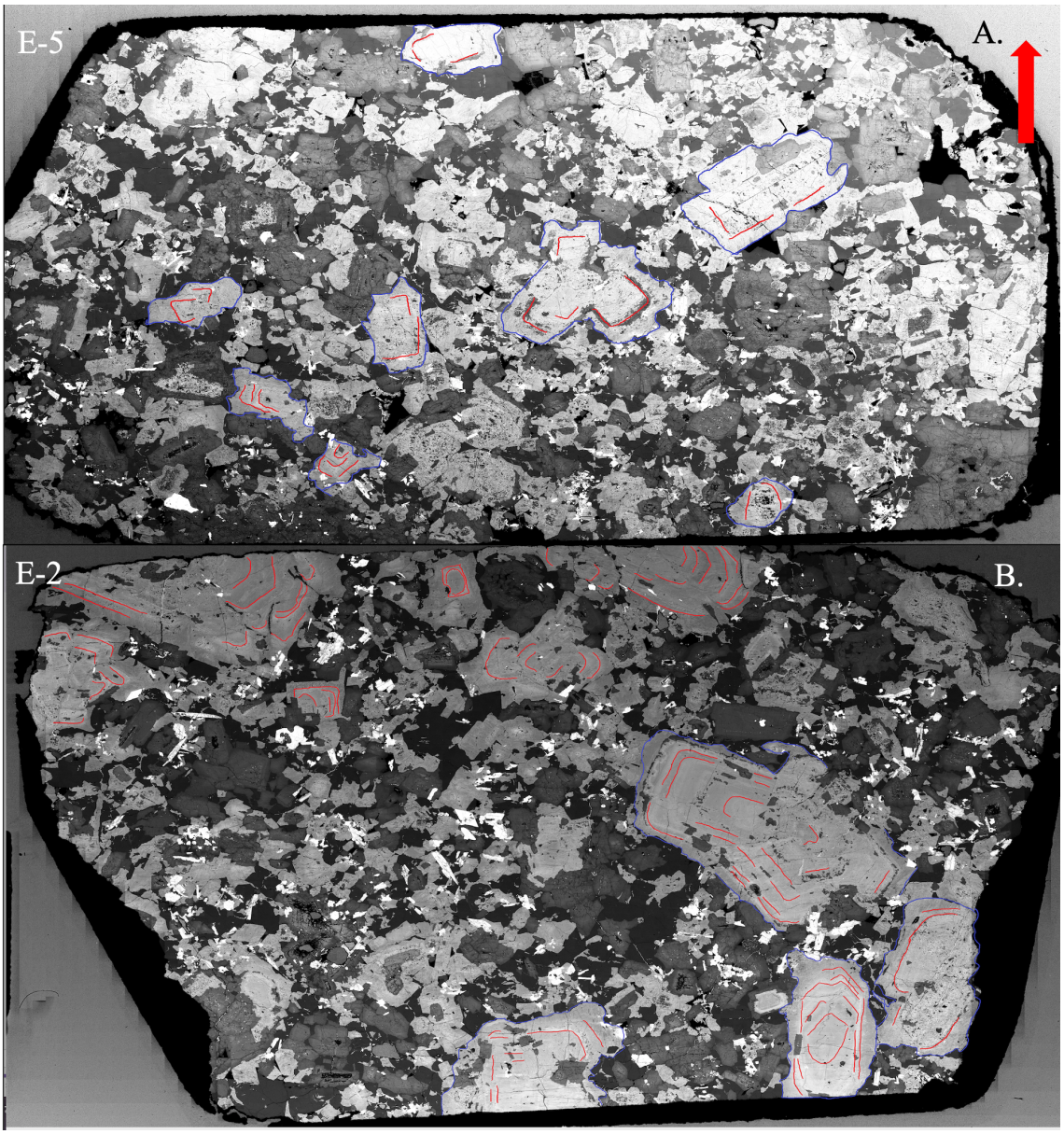

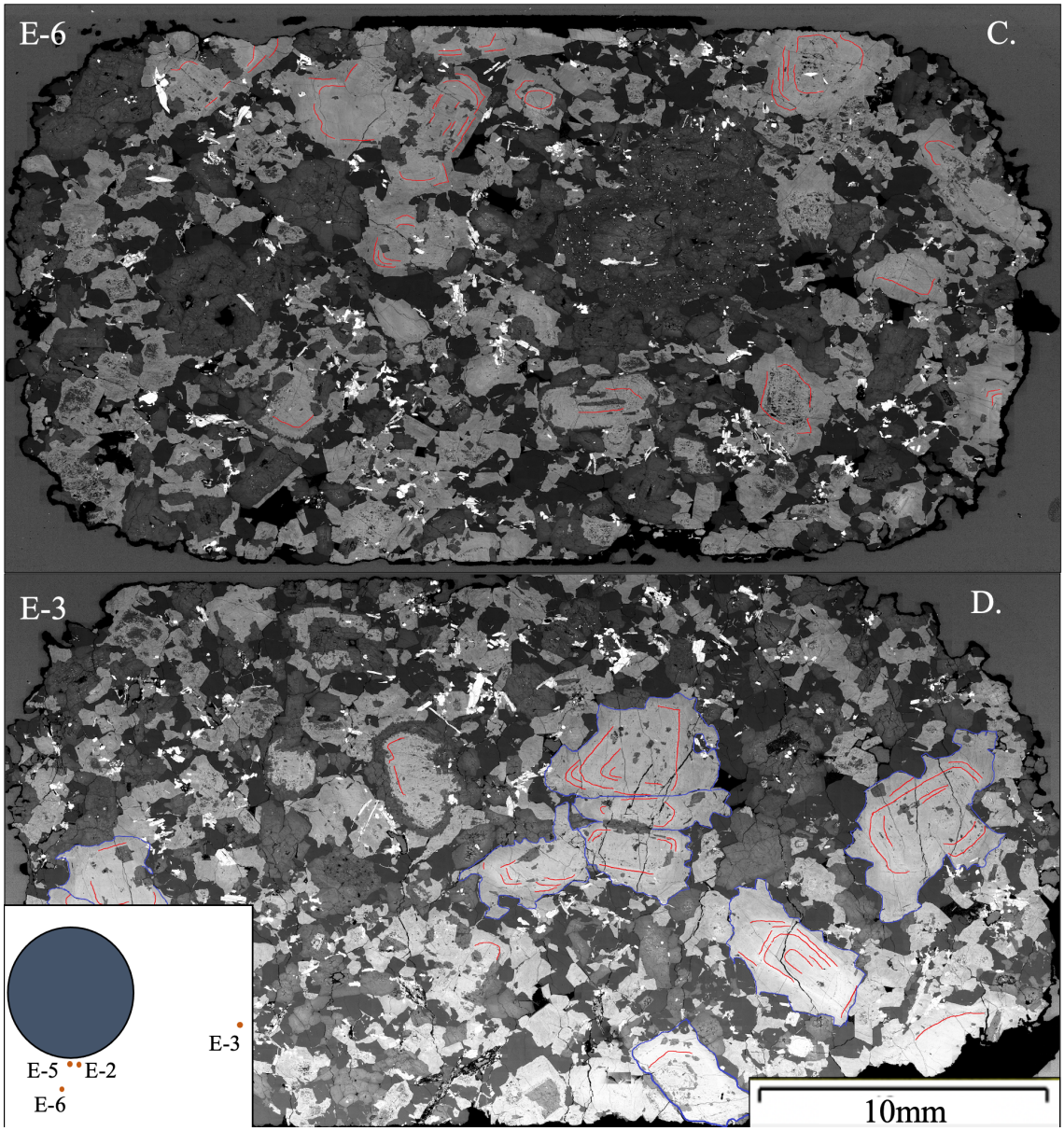

Figure 9: BSE maps of all four thin sections. Some of the visible alkali feldspar zones are outlined in red, and some of the alkali feldspar rims are outlined in blue. Alkali feldspar are lighter gray, plagioclase are medium gray, and quartz are darker gray. A. Map of E-5, located directly underneath the BFE: most alkali feldspar are euhedral with distinct zoning patterns. Plagioclase are generally smaller than the alkali feldspar and quartz is primarily interstitial. B. Map of E-2, located next to E-5 underneath the BFE. Large euhedral alkali feldspar (¡10mm) primarily make up the map. Plagioclase are euhedral, but they are smaller than the alkali feldspar; quartz is interstitial. C. BSE map of E-6, located underneath E-5: alkali feldspar are anhedral; zones are outlined in red. There is a large plagioclase cluster in the center of the sample and there are alkali feldspar grains with distinct plagioclase zones within the grains. D. BSE map of E-3, located in the far field. E-3 is texturally distinct from E-5 and E-2 (both have large euhedral alkali feldspar). The most notable features are the irregular alkali feldspar rims. These rims are tendril-like and are darker grey than the rest of the alkali feldspar grains.

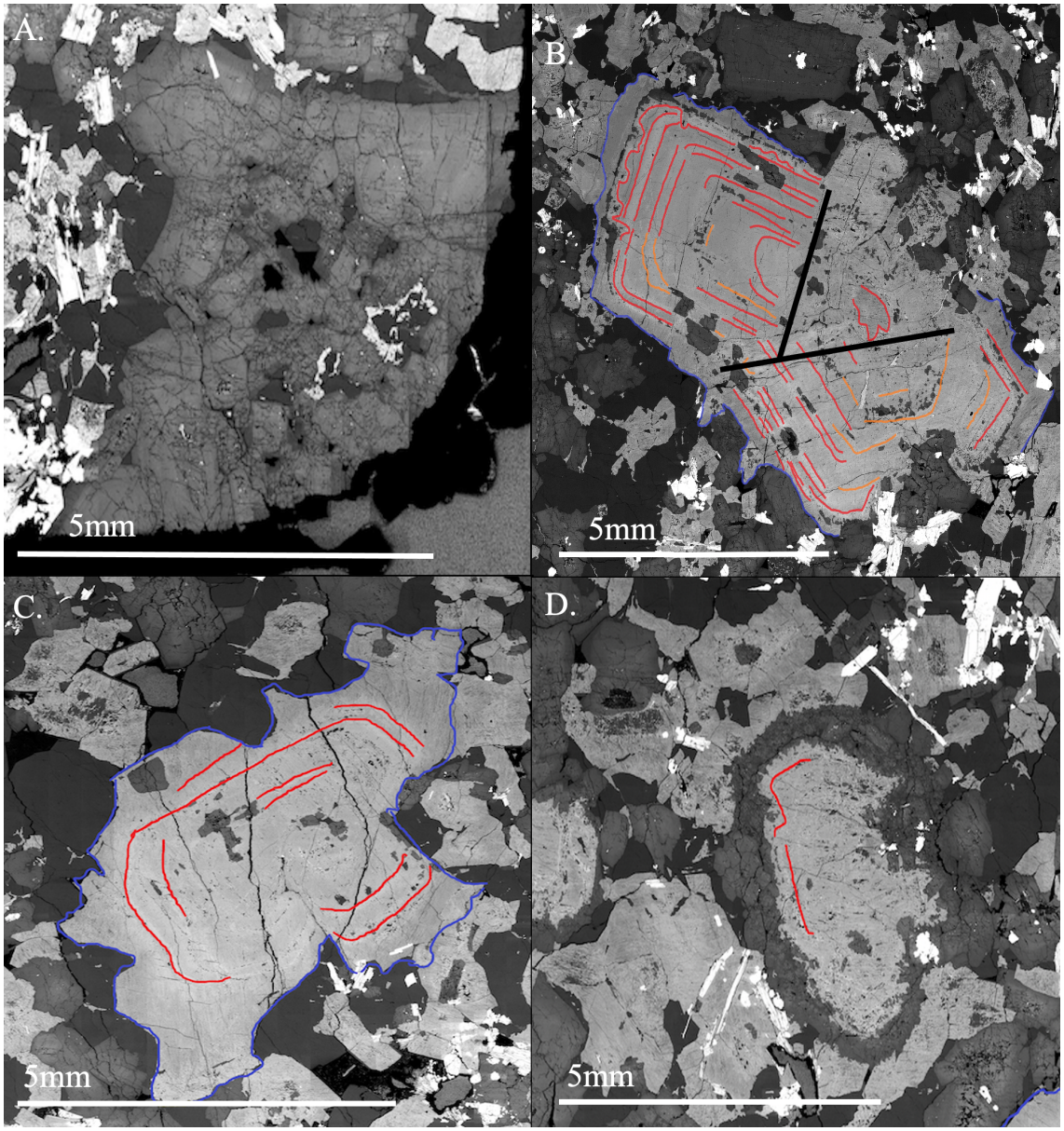

Figure 10: BSE images of four interesting feldspar textures. Internal zoning is outlined in red and rims are outlined in blue. A. Plagioclase cluster in E-5 (directly underneath the enclave) shows bent grains. B. In E-2, a large alkali feldspar grain is broken. We can observe three domains within the grain, with the wedge-shape zone interrupting the zoning seen in the outer domains. C. Example of an irregular alkali feldspar rim in E-3 (located in the far field). There are distinct euhedral zones within the grain, but the rim is irregular with tendrils of material interstitial to matrix grains. This rim texture is abundant in sample E-3, while the euhedral grains (such as the one in 11B) are common in samples E-5 and E-2. In other alkali feldspar in the sample, as well as this example, the rims are darker than the interior of the grain. D. Alkali feldspar with plagioclase zone in E-6 (underneath the E-5). These zones of plagioclase are common in all four of the samples.

3.2 Energy Dispersive Spectrometry (EDS)

False color maps created from the EDS data (Figure 11) highlight and help to identify the different phases present. In this case, K is in the green channel, Na in the blue channel, and Ca in the red channel; the

combination of intensities in the three channels renders alkali feldspar in green shades and renders plagioclase in purple colors. In all the thin section maps, compositional zoning of K and Na can be seen within the alkali feldspar and zoning of Na and Ca is visible in the plagioclase. Plagioclase zoning is more visible in the EDS maps compared to the BSE, while alkali feldspar zoning is more distinct in the BSE maps. The EDS maps clearly show the plagioclase inclusions and plagioclase zones within the alkali feldspar grains as described for the BSE maps. The distinct color difference between the two phases highlights contrasting features, specifically interior plagioclase zones and plagioclase inclusions within the alkali feldspar grains. Additionally, since plagioclase zoning is more visible in these maps, the plagioclase cluster in E-6 shows all the individual grains making up the larger cluster (Figure 11D). It appears that there are several smaller grains in the center and a more intact rim surrounding the whole cluster. EDS is useful for major elements, as well as some trace elements such as Ba (Figure 12). Ba maps potentially show alkali feldspar rims that are depleted in Ba in all of the samples, but this is most prominently seen in E-3 in the irregular rims.

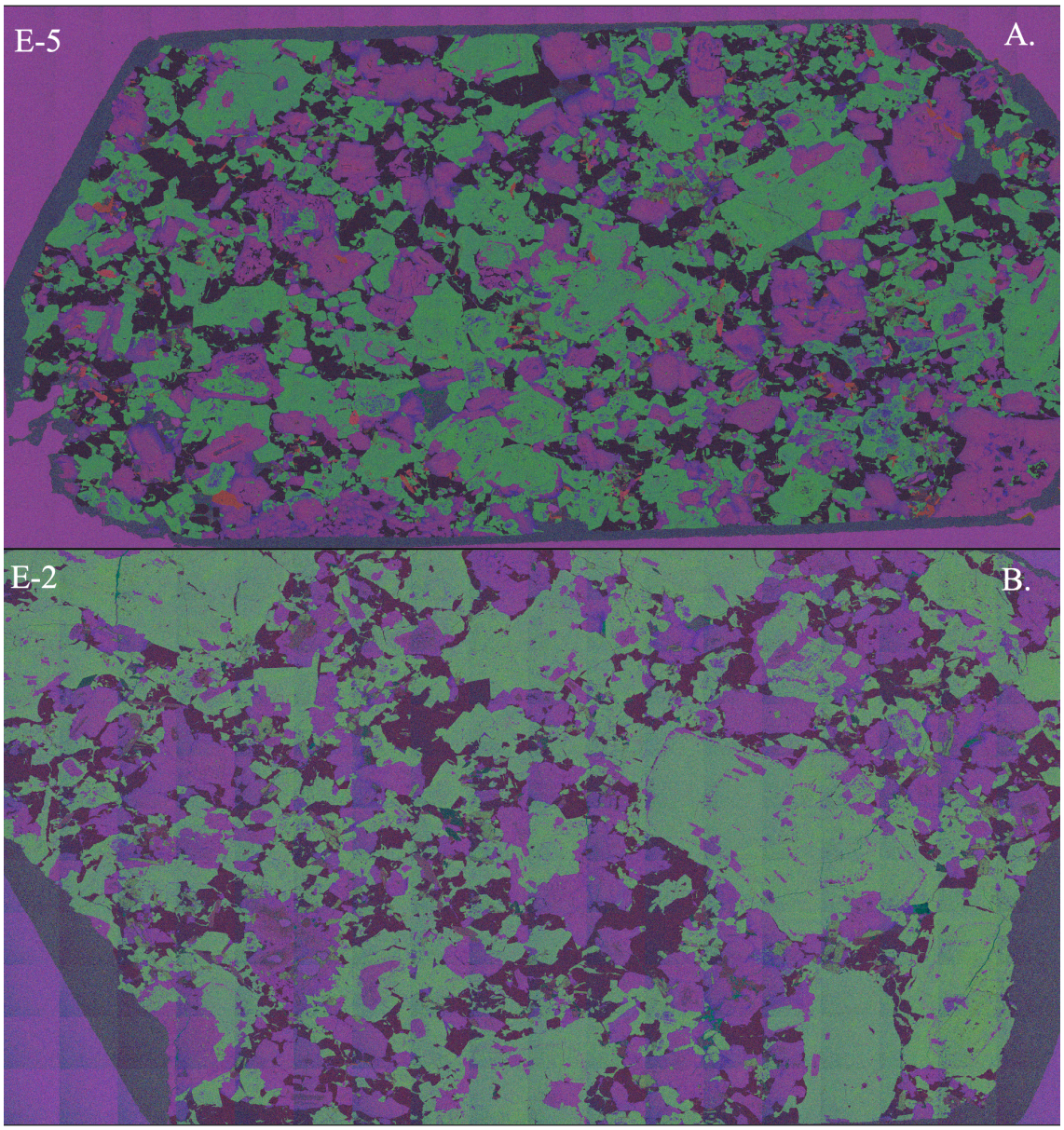
E-5
A.
E-2
B.

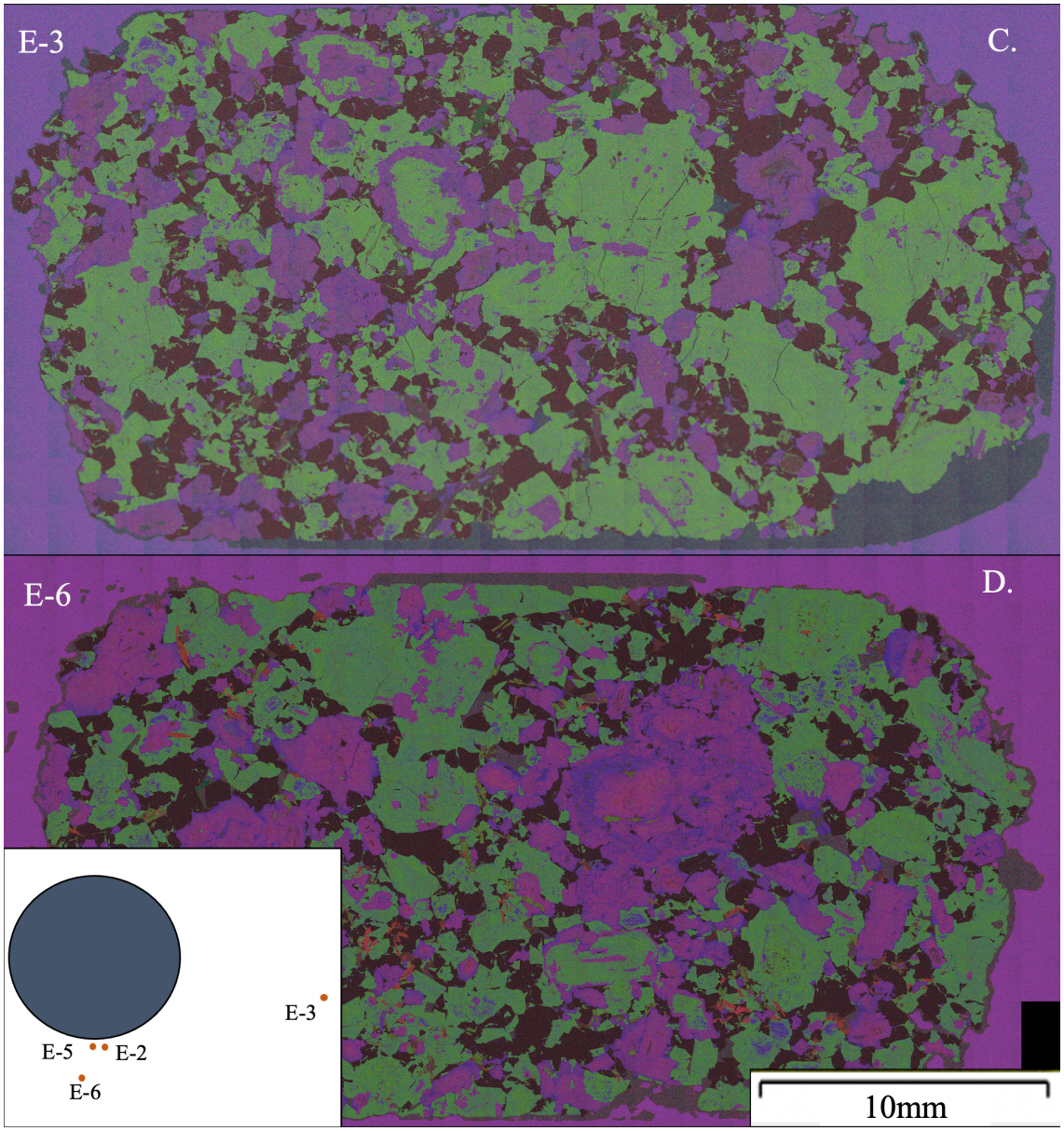

Figure 11: False color EDS map of all four samples. A. E-5, B. E-2, C. E-3, and D. E-6. Alkali feldspar grains are green and plagioclase grains are purple. Zoning can be seen clearly within the plagioclase grains. Alkali feldspar zoning is still visible, but not as clear as in the BSE images. Plagioclase inclusions and zones can be seen clearly in these false color maps. A. In E-5, inclusions and zones of plagioclase can be observed within the euhedral alkali feldspar. B. Alkali feldspar zoning is seen within E-2 in the large euhedral grains along with the plagioclase inclusions and zones seen in other samples. C. In E-3, the irregular rims observed in the BSE image can be seen in this EDS map as well. D. Similarly to the other samples, zoning in E-6 can be observed in this EDS map. Additionally, the large plagioclase cluster in the middle of the image can be seen in greater detail. Individual grains within the cluster are more visible, and we can see a rim surrounding the majority of the cluster that is more Ca-rich.

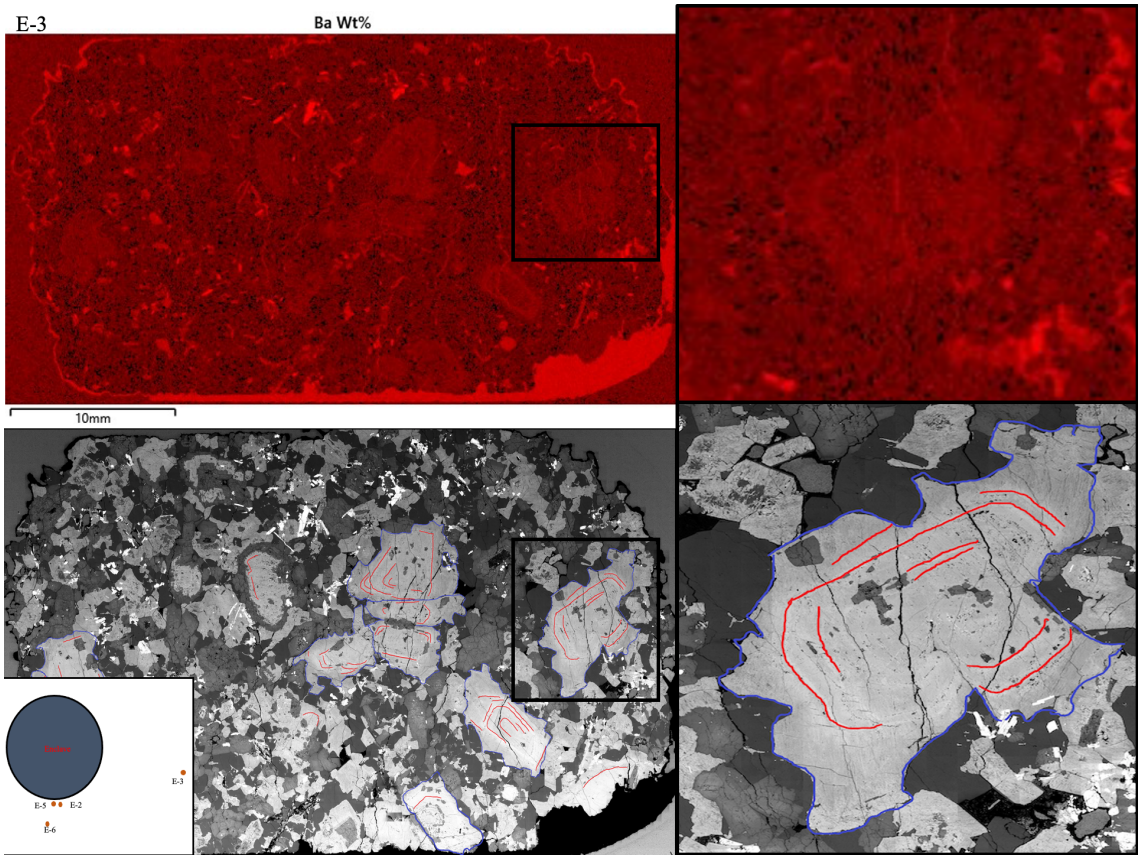

Figure 12: Ba EDS maps and BSE images showing zoning in alkali feldspar in sample E-3. Ba EDS maps on top, in shades of red, while BSE images are on the bottom, in shades of gray. We observe that the BSE dark, irregular rims are Ba-depleted, compared to the Ba-rich, BSE bright cores. This can be seen more clearly in the zoomed-in maps of a large alkali feldspar grain located to the right of the thin section. The zones that are visible and outlined in the BSE map match with the area of the grain that is Ba-rich in the EDS map. These darker rims can in found on the other samples, but they are much smaller and harder to observe with an EDS map.

3.3 Electron Backscattered Diffraction (EBSD)

EBSD thin section maps (Figure 7) can show different important attributes of the samples. Band contrast maps show the individual grains; phase maps show the abundance and distribution of the different minerals (Table 1); Euler maps show the orientations of grains; and the GOS maps reveal intragrain deformation. Besides the qualitative work that can be done with the maps, it is also possible to extract quantitative information on intragrain deformation and crystallographic preferred orientation of different mineral phases.

Sample	Alkali Feldspar (%)	Plagioclase (%)	Quartz (%)	Zero Solutions (%)
E-5	37.5	31.4	26.2	4.4
E-2	40.6	27.9	28.9	2.5
E-3	39.7	28.6	26.2	5.4
E-6	37.7	34	25.2	3.1

Table 1: EBSD mineral percentages.

The GOS angle measures how far the orientation of each pixel within a grain deviates from the average orientation of the grain. Grain diameter on Channel5 is the diameter of a circle fit to individual grains based on their shape and area; the circle approximates the area of each individual grain. It is an approximation for the size of each grain, and it tends to be less dependent on grain aspect ratio. Plots of GOS vs. grain diameter within each sample show the deformation within a grain vs the size of the grain (Figure 13). GOS angles in E-2 have a range from 0-133 degrees; however, all the samples have GOS angles that range up to at least 100 degrees. In all the samples, the smaller grains (¡1 mm diameter) have the maximum range in each sample. These small grains can have very little deformation (small GOS angle) and can be highly deformed (large GOS angle). Most of the grains are less than 1 mm in diameter. Our sample size of large grains (¿2 mm diameter) is small; therefore, any patterns may not be representative of the sample as a whole. In E-3, it does appear that the larger grains generally have GOS angles less than 40 degrees, while E-5, E-6, and E-2 all have larger grains with GOS angles greater than 40 degrees and up to 100 degrees.

Histograms of the angle between vertical and the pole to the (0 1 0) plane are plotted for alkali feldspar in each of the four samples (Figure 14). The histogram for E-5 shows a unimodal, slightly asymmetric distribution with a mean of 12 degrees and a standard deviation of 37 degrees skewed to the right. These data are tightly clustered at 12 degrees, especially compared to the other three samples. E-2 has a symmetric distribution with a mean of 3 degrees and standard deviation of 39 degrees. Histograms for E-3 and E-6 are roughly symmetrical with means of -4.5 and -0.1 respectively, but they appear to be bimodal with peaks at approximately -30 degrees and 45 degrees. Compared to E-2, E-5 has a more pronounced peak with clustered data, but both distributions are unimodal. E-5 has the tightest clustering of data with a standard deviation of 37 compared to the rest of the samples that have means of 39 (E-3), 39 (E-2), and 42 degrees (E-6).

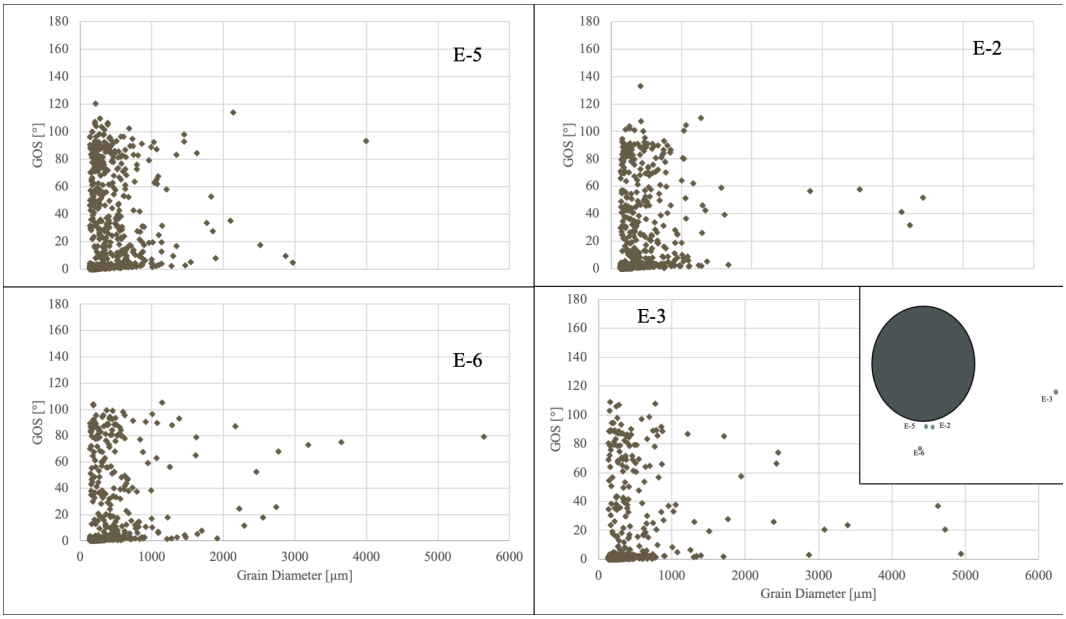

Figure 13: Grain Spread Orientation (GOS) angle vs. grain diameter in alkali feldspar show intragrain deformation in alkali feldspar grains of different sizes for the four samples. GOS measures how much variability in orientation there is within pixels of each grain; a larger angle implies that the grain is more deformed. All the samples look remarkably similar to each other in these plots. While there are a few large grains in E-5 and E-6 that are more deformed, there does not appear to be a great difference. It is important to note that the sample size for the smaller grains is much higher than the large grains and therefore the deformation shown here may not be representative of the granite in each of these locations.

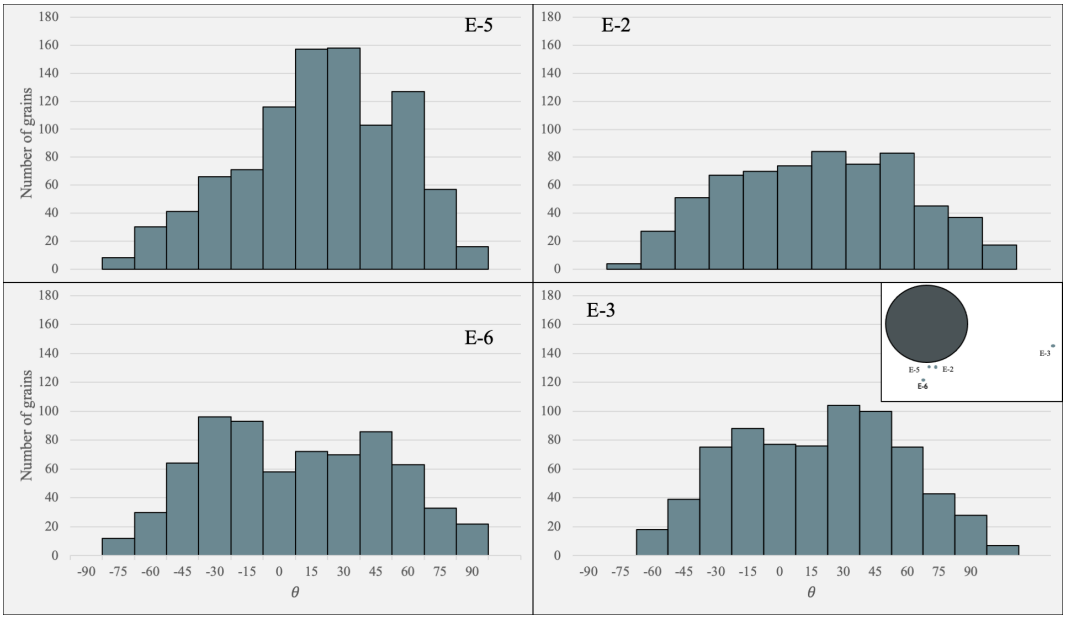

Figure 14: Histograms showing the foliation strength in the four samples. A sample with a strong foliation would have a tightly clustered unimodal distribution of θ, while a sample with no foliation would show a uniform distribution of θ. E-5 has the strongest foliation, while E-2 appears to have a weaker foliation. E-6 and E-3 appear to have a bimodal distribution; however, further statistical analysis must be done to confirm this pattern. Interestingly, each sample is foliated, with E-5 having the strongest foliation.

CHAPTER 4

Discussion

4.1 Evidence of deformation

Deformation of mineral grains occurred underneath the enclave. Bent and broken crystals can be used as evidence of deformation of the magma mush (Philpotts et al., 1996). In the samples located directly underneath the enclave (E-5 and E-2), deformation of grains is confirmed with multiple methodologies. In the BSE map of E-2, a large euhedral alkali feldspar shows a curved grain shape (Figure 15A). The zoning patterns within the grain are offset in the middle of the feldspar. Additionally, the rim appears to be continuous and to lack this offset. This mismatch can also be seen in the EDS maps, with the zoning patterns appearing more distinct in the lower half of the grain, compared to the upper half (Figure 15B). While the BSE and EDS maps show the qualitative difference in zoning patterns, the EBSD Euler map quantitatively shows that the orientations of the lower half and the upper half of the grain are distinct and that there is a sharp boundary between the two domains of the grain with a misorientation of 85° (Figure 15C). Note that there is also a twinning relationship shown in this grain within the lower boundary with a misorientation of 177°. However, this orientation difference is not indicative of deformation, rather being typical crystal growth (Deer, Howie, and Zussman 2013, p. 266-267). Additionally, there are three distinct domains shown in the EBSD GOS map in between the two halves of the grain that have very little intragrain deformation (Figure 15D). This low degree of intragrain deformation may indicate that the three domains between the two broken halves may be new growth after the initial breakage. Pairing the BSE, EDS, and EBSD maps, it is evident that this grain is broken, indicating that brittle deformation occurred in the magma mush. A plagioclase cluster located in E-5 shows more evidence of brittle deformation occurring in the mush directly underneath the enclave (Figure 16). There are three domains within a crystal within this cluster that have distinct orientations: the misorientation between first and second domains is 146° and the misorientation between the second and the third domains is 132°. No bent or broken grains are observed in either E-6 or E-3, the samples located further away from the enclave.

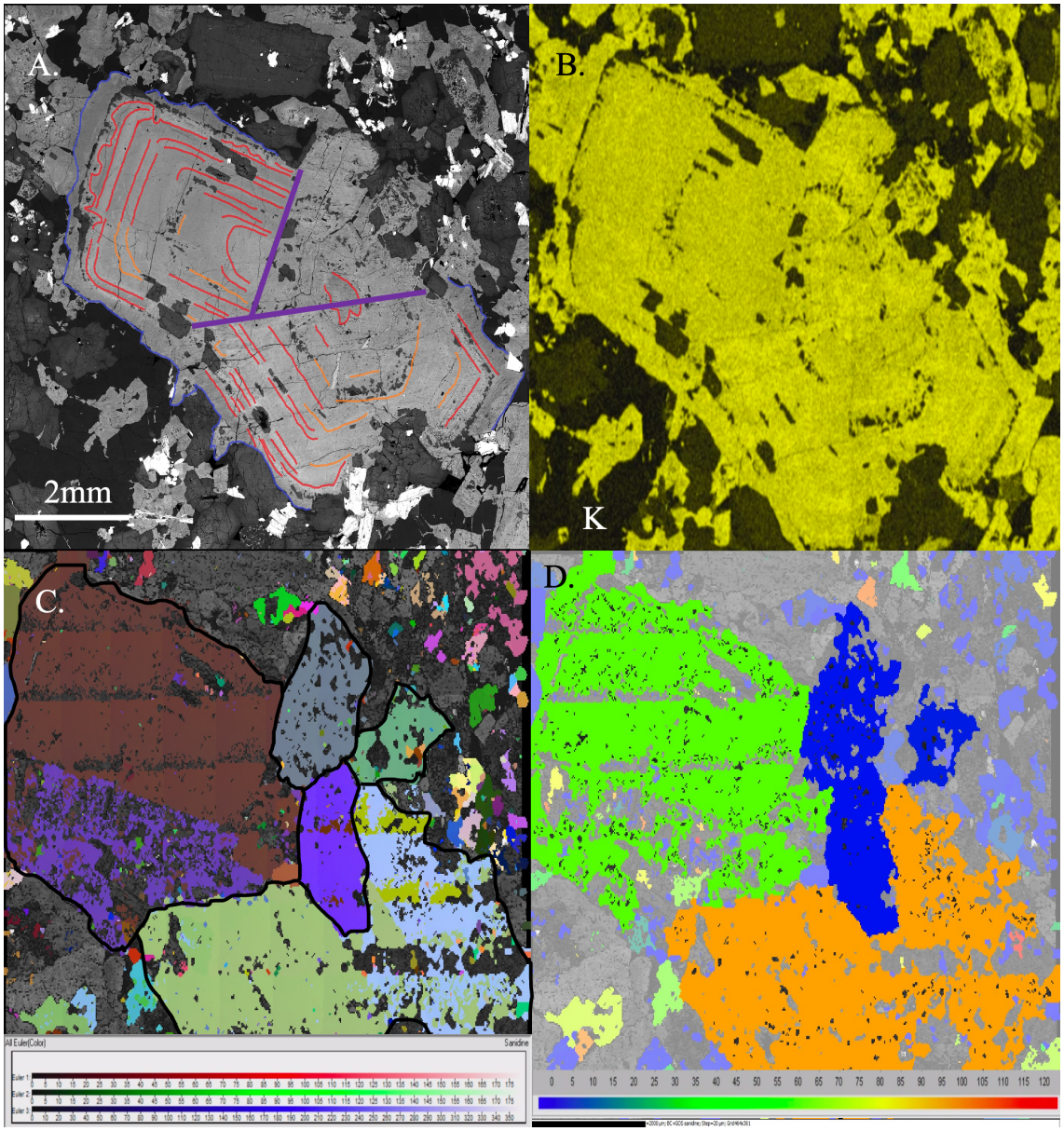

Figure 15: Analysis of the bent grain in E-2 with BSE (A), EDS (B), Euler angles (C), and GOS (D). All four visualizations of this large grain show that there are different domains. The Euler map (C) shows that the different domains observed in the BSE image are true orientation differences. The different orientation domains are outlined in black. Note that there is twinning occurring in the top domain (brown/purple) and the lower domain (green/blue); these orientation differences are due to normal crystal growth, not deformation. The GOS map (D) also shows the different domains. The lower domain is the most deformed, with three areas within the wedge of the two main domains having no intragrain deformation. This data shows that the grain broke, and new growth (3 wedge domains) may have occurred after the breakage.

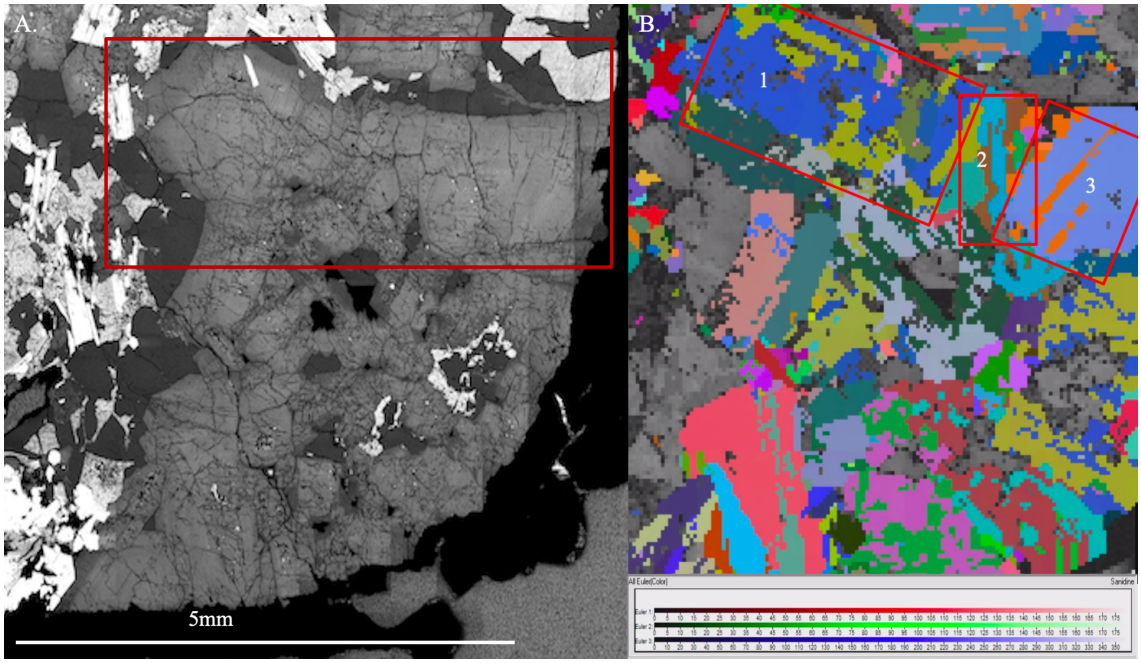

Figure 16: BSE (A) and Euler (B) maps of plagioclase cluster in E-5 showing the three different orientation domains in the top plagioclase grain, indicating that this grain broke into three pieces. Other bent grains within the cluster do not have subgrains within them and may have undergone ductile rather than brittle deformation.

Intragrain deformation of different mineral phases can also indicate mush deformation (Philpotts et al., 1996; Holness et al., 2019). In this granitic magma, we infer that feldspars (both alkali feldspar and plagioclase) saturated and began to grow early, while quartz, which is interstitial, saturated later than feldspars. Texturally, quartz grains are typically interstitial between euhedral crystals of both feldspars. Quartz grains do not show visible signs of being broken; therefore, we assert that quartz had not saturated at the moment the feldspar breakage happened. This can be further confirmed using GOS data from the EBSD. GOS shows the amount of intragrain deformation for each individual grain of the thin section. The thin section maps demonstrate that the alkali feldspar grains more commonly have intragrain deformation than the quartz grains, consistent with the inference that quartz saturated after the deformation of the feldspars (Figure 17). These lines of evidence indicate that quartz grains formed after the enclave impinged on the magma mush, which shows that deformation happened in the presence of melt. However, it is interesting to note that quartz grains do show some level of deformation. This may be because quartz grains are relatively easy to deform, which again confirms that quartz is a late-stage phase because we would expect it to be significantly more deformed than the feldspars due to its lattice structure (Karlstrom, 1993; McCaffrey et al., 1999). While comparison of GOS angles between the different thin sections do not show any clear patterns, these data do provide evidence that there was ductile deformation occurring while this mush was forming, specifically in

the alkali feldspar grains versus the quartz grains. Evidence of deformation can lead to further implications about the rheology of the system and what processes were occurring, such as compaction and melt extraction.

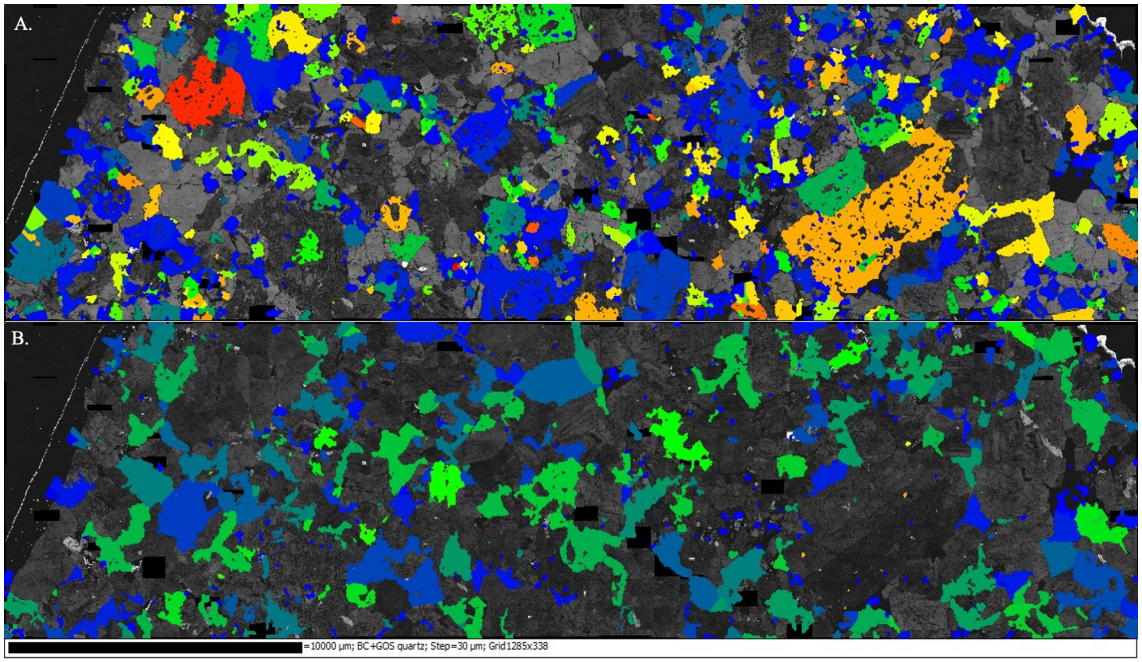

Figure 17: GOS map of E-5 showing intragrain deformation in alkali feldspar grains (A) vs. quartz grains (B). The alkali feldspar grains have more intragrain deformation than the quartz grains. This difference indicates that quartz grew after the feldspar were deformed.

4.2 Compaction beneath the BFE

Evidence of deformation and foliation patterns within this granite indicates that compaction occurred when the magma was a mush with developed feldspar crystals and when quartz had not crystallized yet. This compaction can be connected to the impingement of the enclave into the mush based on the variation in the strength of the fabric as a function of the location of the samples relative to the enclave. Mush compaction can be defined by several different processes such as gravitational loading, viscous deformation, or mechanical rearrangement of mineral grains, but clearly identifying compaction as well as its source is challenging (Bachmann and Bergantz, 2004; Holness et al., 2019; Philpotts et al., 1996). Foliation of minerals has been tied to mechanical mush compaction, where grains are physically rearranged in a mush in a magmatic flow regime (Holness et al., 2019). While foliations can be very informative, constraining the state of the magma mush through the preserved fabric is challenging because it is difficult to clearly tie the fabric to stress (Mader et al., 2013). In the case of the BFE, the strength of the foliation as well as the proximity to the enclave show both evidence of compaction, as well as the direct source of compaction. In E-5, we see a strong signature of the foliation directly underneath the enclave, while E-2, E-3, and E-6 all show a much weaker signal indicating that the BFE is the source of compaction (Figure 14).

In the Aztec Wash pluton, alkali feldspar is the primary fabric-forming mineral. Histograms of θ (the angle between paleovertical and the (010) plane) in the alkali feldspar show the strength of foliation within each sample (Figure 14). As previously stated in the methods, a strong foliation should be represented by a tightly clustered normal distribution of θ, while no foliation should have a randomly distributed histogram. In this case, E-5, located directly underneath the enclave, has the strongest foliation, concurring with initial field observations of an observed fabric. All these sample distributions are approximately centered on zero, but there is some difference between the samples. In E-5, the peak is located closer to 15 degrees, which is consistent with the tilting of this section of the Aztec Wash pluton. At the location of the BFE, the plutonic blocks are tilted by 15 degrees to the WSW (Harper et al., 2004). Additionally, it appears that all the samples have some degree of foliation; none of these distributions show completely random alignment. A sample with no foliation would have a uniform distribution of the (0 1 0) poles. This may be due to a naturally occurring fabric within the magma mush rather than the enhanced fabric due to the BFE. Comparing the extent of foliation to intragrain deformation (as indicated by GOS) may provide a means of differentiating between normally occurring crystal alignment in a mush, versus forced compaction via the enclave; a lesser degree of foliation paired with less intragrain deformation may indicate normal crystal alignment.

4.3 Length scale of compaction

While the strength of the foliation (as measured by the distribution of poles to the (0 1 0) plane of alkali feldspar) varies as a function of location relative to the BFE, it can also demonstrate the length scale of compaction. Although it appears that sample E-5 has the strongest fabric, E-2 (also located directly underneath the enclave) has a similar pattern (Figure 14). Contrastingly, while both samples located further away (E-3 and E-6) have some preferred orientation, the distributions have a different pattern than E-5 and E-2; they appear to be bimodal. These are preliminary data and further statistical analysis of these histograms will provide more complete and detailed comparisons of these distributions. Sample E-3 gives a reference for the extent of foliation in the far field, and, thus, E-5 and E-6 are a good measure of the vertical extent of the foliation and how far down the BFE compacted the mush. E-5 is located 0.25 m underneath the enclave and E-6 is located 0.5 m underneath. This distance between the enclave and E-6 can give us an estimate of the length scale of compaction and it can inform future sampling and exploration of the compaction scale to help us further understand the rheology of the magma mush. Additionally, looking at the mineral abundances and intragrain deformation can indicate whether E-2 is representative of the horizontal length scale of compaction and to understand the extent of melt extraction surrounding the BFE. E-2 may be representative since it has a weaker foliation signature than E-5.

4.4 Evidence of melt extraction

The evidence of compaction can be paired with evidence of melt extraction that can further indicate that a mush was deformed by the enclave. Melt extraction is of particular interest because it ties into a main question in the study of volcanoes: how do we generate large bodies of eruptible, crystal-poor material (Bachmann et al., 2007)? The reason this enclave represents a unique opportunity is because it presents a snapshot of the magma mush system in the Aztec Wash pluton. If we can constrain both the crystal deformation as well as how much melt was extracted, we will have a better understanding of the rheology of the magmatic system at the moment of enclave impact.

Pairing both the BSE images and EDS maps, we can begin to evaluate whether melt extraction occurred and constrain how much melt was extracted. BSE maps of E-5 and E-2, samples located directly underneath the enclave, show large alkali feldspar grains that are euhedral (Figure 10A and B). Especially in the case of E-2, there are several large alkali feldspars with euhedral rims that follow the zoning patterns of the grains. In contrast, in E-3 and E-6, samples located in the far field and further underneath from the enclave, respectively, the alkali feldspar grains have rims that are irregular, with regular zoning patterns observed within the grains (See Figure 10B and 10C for rim comparison). In E-3, these irregular rims are prominent, especially in the large grains. The samples close to the enclave have euhedral grains, while samples far away from the enclave have irregular rims. This suggests that melt was extracted from underneath the enclave; the irregular rims represent melt that would have been extracted. Furthermore, the irregular rims in E-3 are all darker gray in the BSE maps, indicating a compositional change (Figure 10C). Calculating the area of these rims with different color and shape will help estimate how much melt was extracted from underneath the enclave, as well as looking at quartz abundance. While E-5 and E-3 (underneath the BFE vs the far field) have similar quartz abundances around 26%, E-2 (offset from E-5 underneath the BFE) has slightly more quartz at almost 29% abundance (Table 1). This may indicate some melt movement around the BFE since quartz was saturated after the deformation, however the differences in abundance are quite small. Additionally, using EDS maps to look at the composition of the irregular rims will help constrain the system further. The darker rims of the alkali feldspars in the BSE maps correspond to depleted Ba (Figure 12). Using both the EDS maps and the BSE maps to calculate the area will make these analyses more precise. This evidence further supports that the enclave deformed the mush, causing the melt to be extracted. Although further analysis is needed, the evidence of compaction and melt extraction in the mush surrounding the enclave is an important start.

CHAPTER 5

Conclusions

In the cumulate granite of the Aztec Wash pluton, we can start to constrain the state of the magma mush due to the presence of the BFE. Deformed grains, strong foliation, and the differences in rim shape between the samples directly underneath the enclave (E-5 and E-2) and the samples located further away (E-3 and E-6) indicate that compaction and melt extraction occurred underneath the enclave. Furthermore, we may be able to constrain the length scale of deformation induced by the enclave at 0.5 m below the BFE as E-6 does not have the same evidence of deformation as E-5 and E-2. This enclave represents the boundary between a crystal-rich and crystal-poor region of the magma body at the time of emplacement, and the textures in the granite surrounding the enclave allow us to understand how the BFE deformed this mush at the boundary. Future work will focus on constraining the amount of melt extracted and further understanding of the foliation underneath the enclave. In addition, I will be completing analog experiments simulating the enclave falling into a magma mush. These experiments will be imaged using a CT to show the 3D rearrangement of grains in the mush.

References

Bachmann, O. and Bergantz, G. (2004). On the origin of crystal-poor rhyolites: Extracted from batholithic crystal mushes. *Journal of Petrology*, 45(8):1565–1582.

Bachmann, O., Miller, C., and de Silva, S. L. (2007). The volcanic–plutonic connection as a stage for understanding crustal magmatism. *Journal of Volcanology and Geothermal Research*, 167(1-4):1–23.

Beane, R. and Wiebe, R. (2012). Origin of quartz clusters in vinalhaven granite and porphyry, coastal maine. *Contributions to Mineralogy and Petrology*, 163(6):1069–1082.

Cates, N., Miller, J., Miller, C. F., Wooden, J., Ericksen, S., and Molly, M. (2003). Longevity of plutonic systems: Shrimp evidence from aztec wash and searchlight plutons, nevada. *Geological Society of America Abstracts with Programs*, 35(4).

Coussot, P. and Ancey, C. (1999). Rheophysical classification of concentrated suspensions and granular pastes. *Physical Review E*, 59(4):4445–4457.

Deer, W., Howie, W., and Zussman, J. (2013). *An Introduction to the Rock-Forming Minerals*, The Mineralogical Society, 3rd edition:266–267.

Falkner, C., Miller, C., Wooden, J., and Heizler, M. (1995). Petrogenesis and tectonic significance of the calc-alkaline, bimodal aztec wash pluton, eldorado mountains, colorado river extensional corridor. *Journal of Geophysical Research: Solid Earth*, 100(B6):10453–10476.

Faulds, J., Feuerbach, D., Miller, C., and Smith, E. (2001). Cenozoic evolution of the northern colorado river extensional corridor, southern nevada and northwest arizona. *Geological Association Publication 30 - Pacific Section American Association Petroleum Geologists Publications*, GB78:239–271.

Giordano, D., Mangiacapra, A., Potuzak, M., Russell, J., Romano, C., Dingwell, D., and Muro, A. D. (2006). An expanded non-arrhenian model for silicate melt viscosity: A treatment for metaluminous, peraluminous and peralkaline liquids. *Chemical Geology,*, 229(1):42–56.

Giordano, D., Russell, J., and Dingwell, D. (2008). Viscosity of magmatic liquids: A model. *Earth and Planetary Science Letters*, 271(1):123–134.

Graeter, K., R.Beane, Deering, C., Gravley, D., and Bachmann, O. (2015). Formation of rhyolite at the okataina volcanic complex, new zealand: New insights from analysis of quartz clusters in plutonic lithics. *American Mineralogist*, 100(8-9):1778–1789.

Harper, B., Miller, C., Koteas, G., Cates, N., Wiebe, R., Lazzareschi, D., and Cribb, J. (2004). Granites, dynamic magma chamber processes and pluton construction: The aztec wash pluton, eldorado mountains, nevada, usa. *Earth and Environmental Science Transactions of The Royal Society of Edinburgh*, 95(1-2):277–295.

Hess, K. and Dingwell, D. (1996). Viscosities of hydrous leucogranitic melts: A non-arrhenian model. *American Mineralogist*, 81(9-10):1297–1300.

Hildreth, W. (2004). olcanological perspectives on long valley, mammoth mountain, and mono craters: Several contiguous but discrete systems. *Journal of Volcanology and Geothermal Research*, 136(3):169–198.

Holness, M. (2018). Melt segregation from silicic crystal mushes: A critical appraisal of possible mechanisms and their microstructural record. *Contributions to Mineralogy and Petrology,*, 173(6):48.

Holness, M., Stock, M., and Geist, D. (2019). Magma chambers versus mush zones: Constraining the architecture of sub-volcanic plumbing systems from microstructural analysis of crystalline enclaves. *Philosophical Transactions. Series A, Mathematical, Physical, and Engineering Sciences*, 377(2139).

Ji, S., Shao, T., Salisbury, M., Sun, S., Michibayashi, K., Zhao, W., Long, C., Liang, F., and Satsukawa, T. (2014). Plagioclase preferred orientation and induced seismic anisotropy in mafic igneous rocks: Plagioclase and seismic anisotropy. *Journal of Geophysical Research: Solid Earth*, 119(11):8064–8088.

J.J.Stickel and Powell, R. (2005). Fluid mechanics and rheology of dense suspensions. *Annual Review of Fluid Mechanics*, 37(1):129–149.

Karlstrom, K. (1993). Pluton emplacement along an active ductile thrust zone, piute mountains, southeastern california: Interaction between deformationai and solidification processes. *Geological Society of America Bulletin*, 18.

Lazzareschi, D. (2004). Fine-grained felsic enclaves in the cumulate granite zone of the aztec wash pluton, nevada. pomona college, undergraduate honors thesis.

Leigh, M., Miller, J., and Blackburn, T. (2018). Timescale for the construction of aztec wash pluton, southern nevada. geological society of america. *Abstracts with Program*, 50(6):–.

Mader, H., Llewellin, E., and Mueller, S. (2013). The rheology of two-phase magmas: A review and analysis. *Journal of Volcanology and Geothermal Research*, 257:135–158.

Marsh, B. (1981). On the crystallinity, probability of occurrence, and rheology of lava and magma. *Contributions to Mineralogy and Petrology*, 78(1):85–98.

McCaffrey, K., Miller, C., Karlstrom, K., and Simpson, C. (1999). Synmagmatic deformation patterns in the old woman mountains, se california. *Journal of Structural Geology*, 21(3):355–349.

Miller, C. and Miller, J. (2002). Contrasting stratified plutons exposed in tilt blocks, eldorado mountains, colorado river rift, nv, usa. *Lithos*, 61:209–224.

Miller, C., Miller, J., and Faulds, J. (2005). Miocene volcano-plutonic systems, southern nevada: A window into upper crustal magmatic processes: in stevens, c., and cooper, c., eds., western great basin geology: Fieldtrip guidebook and volume, gsa cordilleran section (pacific section sepm, pub.). 99:37–66.

Miller, C., Watson, E., and Harrison, T. (1988). Perspectives on the source, segregation and transport of granitoid magmas. *Earth and Environmental Science Transactions of the Royal Society of Edinburgh*, 79(2-3):135–156.

Mueller, S., Llewellin, E., and Mader, H. (2011). The effect of particle shape on suspension viscosity and implications for magmatic flows. *Geophysical Research Letters*, 38(13).

Philpotts, A., Carroll, M., and Hill, J. (1996). Crystal-mush compaction and the origin of pegmatitic segregation sheets in a thick flood-basalt flow in the mesozoic hartford basin, connecticut. *Journal of Petrology*, 37(4):811–836.

Prior, D., Boyle, A., Brenker, F., Cheadle, M., Day, A., Lopez, G., Peruzzi, L., Potts, G., Reddy, S., Spiess, R., Timms, N., Trimby, P., Wheeler, J., and Zetterstrom, L. (1999). The application of electron backscatter diffraction and orientation contrast imaging in the sem to textural problems in rocks. *American Mineralogist*, 84(11-12):1741–1759.

Saar, M., Manga, M., Cashman, K., and Fremouw, S. (2001). Numerical models of the onset of yield strength in crystal–melt suspensions. *Earth and Planetary Science Letters*, 187(3-4):367–379.

Webb, S. and Dingwell, D. (1990). The onset of non-newtonian rheology of silicate melts: A fiber elongation study. *Physics and Chemistry of Minerals*, 17(2).

Weinberg, R., Vernon, R., and Schmeling, H. (2021). Processes in mushes and their role in the differentiation of granitic rocks. *Earth-Science Reviews*, 220:103665.

Wiebe, R., Wark, D., and Hawkins, D. (2007). Insights from quartz cathodoluminescence zoning into crystallization of the vinalhaven granite, coastal maine. *Contributions to Mineralogy and Petrology*, 154(4):439–453.

Wiebe, R. and W.J.Collins (1998). Depositional features and stratigraphic sections in granitic plutons: Implications for the emplacement and crystallization of granitic magma. *Journal of Structural Geology*, 20(9):1273–1289.

Žák, J., Verner, K., and Týcová, P. (2008). Grain-scale processes in actively deforming magma mushes: New insights from electron backscatter diffraction (ebsd) analysis of biotite schlieren in the jizera granite, bohemian massif. *Lithos*, 106(3-4):309–322.